

1 **ShellChron 0.4.0: A new tool for constructing chronologies in accretionary carbonate archives**
2 **from stable oxygen isotope profiles**

3 Niels J. de Winter^{1,2}

4 ¹Department of Earth Sciences, Utrecht University, Utrecht, the Netherlands

5 ²AMGC research group, Vrije Universiteit Brussel, Brussels, Belgium

6

7 Corresponding author: Niels J de Winter (n.j.dewinter@uu.nl)

8

9

10

11 **Abstract**

12 This work presents ShellChron, a new model for generating accurate internal age-models for high-
13 resolution paleoclimate archives, such as corals, mollusk shells and speleothems. Reliable sub-annual
14 age models form the backbone of high-resolution paleoclimate studies. In absence of independent sub-
15 annual growth markers in many of these archives, the most reliable method for determining the age of
16 samples is through age modelling based on stable oxygen isotope or other seasonally controlled proxy
17 records. ShellChron expands on previous solutions to the age model problem by fitting a combination
18 of a growth rate and temperature sinusoid to model seasonal variability in the proxy record in a sliding
19 window approach. This new approach creates smoother, more precise age-distance relationships for
20 multi-annual proxy records with the added benefit of allowing assessment of the uncertainty on the
21 modelled age. The modular script of ShellChron allows the model to be tailored to specific archives,
22 without being limited to oxygen isotope proxy records or carbonate archives, with high flexibility in
23 assigning the relationship between the input proxy and the seasonal cycle. The performance of
24 ShellChron in terms of accuracy and computation time is tested on a set of virtual seasonality records
25 and real coral, bivalve-mollusk and speleothem archives. The result shows that several key
26 improvements in comparison to previous age model routines enhance the accuracy of ShellChron on
27 multi-annual records while limiting its processing time. The current full working version of ShellChron

28 enables the user to model the age of a 10-year long high-resolution (16 samples/yr) carbonate records
29 with monthly accuracy within one hour of computation time on a personal computer. The model is freely
30 accessible on the CRAN database and GitHub. Members of the community are invited to contribute by
31 adapting the model code to suit their research topics [and encouraged to cite the original work of Judd](#)
32 [et al. \(2018\) alongside this work when using ShellChron in future studies.](#)

33

34

35 **1. Introduction**

36 Fast growing carbonate archives, such as coral skeletons, mollusk shells and speleothems, contain a
37 wealth of information about past and present climate and environment (e.g. Urban et al., 2000; Wang et
38 al., 2001; Steuber et al., 2005; Butler et al., 2013). Recent advances in analytical techniques have
39 improved our ability to extract this information and obtain records of the conditions under which these
40 carbonates precipitated at high temporal resolutions, often beyond the annual scale (Treble et al., 2007;
41 Saenger et al., 2017; Vansteenberge et al., 2019; de Winter et al., 2020a; [Ivany and Judd, 2022](#)). Key
42 to the interpretation of such records is the development of reliable chemical or physical proxies for
43 climate and environmental conditions which can be measured on a sufficiently fine scale to allow
44 variability to be reconstructed at the desired time resolution. Examples of suitable proxies include
45 observations of variability in carbonate fabric and microstructure and in (trace) elemental and isotopic
46 composition (Frisia et al., 2000; Lough, 2010; Ullmann et al., 2010; Schöne et al., 2011; Ullmann et al.,
47 2013; Van Rampelbergh et al., 2014; de Winter et al., 2017). The unique preservation potential of
48 carbonates in comparison with archives of climate variability at similar time resolutions, such as tree ring
49 records and ice cores, now allows us to recover information about climate and environment of the
50 geological past from these proxies on the (sub-)seasonal scale (Ivany and Runnegar, 2010; Ullmann
51 and Korte, 2015; Vansteenberge et al., 2016; de Winter et al., 2018; 2020b; c; Mohr et al., 2020). The
52 importance of this development cannot be overstated because variability at high (daily and seasonal)
53 resolution constitutes the most significant component of climate variability (Mitchell, 1976; Huybers and
54 Curry, 2006; Zhu et al., 2019; [von der Heydt et al., 2021](#)). Accurate reconstructions of this type of
55 variability are therefore fundamental to our understanding of Earth's climate system and critical for
56 projecting its behavior in the future under anthropogenic global warming conditions (IPCC, [2018](#)[2021](#)).

57 A reliable age model is crucial to for the interpretation of high-resolution carbonate records. An age model
58 is defined as a set of rules or markers that allows the translation of the location of a measurement or
59 observation on the archive to the time at which the carbonate was precipitated. This translation is
60 required for aligning records from multiple proxies or archives to on a common time axis. Age alignment
61 enables data to be intercomparable and to be interpreted in the context of processes playing a role at
62 similar timescales. Age models are based on knowledge about the growth or accretion rate of the archive
63 through time. Many high-resolution carbonate archives contain growth markers on which age models
64 can be based (e.g. Jones, 1983; Le Tissier et al., 1994; Verheyden et al., 2006). These are especially
65 valuable in some mollusk species, in which growth lines demarcate annual, daily, or even tidal cycles
66 (e.g. *Arctica islandica*, Schöne et al., 2005; *Pecten maximus*, Chavaud et al., 2005 and *Cerastoderma*
67 *edule*, Mahé et al., 2010). However, in many mollusk species and most carbonate archives, such
68 independent growth indicators are absent or too infrequent to (relatively) date high-resolution
69 measurements (Judd et al., 2018; Huyghe et al., 2019). In such cases, age models need to be based
70 on alternative indicators.

71 The oxygen isotope composition of carbonates ($\delta^{18}\text{O}_c$) is closely dependent on the isotopic composition
72 of the fluid ($\delta^{18}\text{O}_w$) and the temperature at which the carbonate is precipitated (Urey, 1948; McCrea,
73 1950; Epstein et al., 1953). In most natural surface environments, either one or both factors is strongly
74 dependent on the seasonal cycle, one generally being dominant over the other. This causes carbonates
75 precipitated in these environments to display strong quasi-sinusoidal variations in $\delta^{18}\text{O}_c$ that follow record the
76 seasonal cycle (e.g. Dunbar and Wellington, 1981; Jones and Quitmyer, 1996; Baldini et al., 2008).
77 Examples of this behavior include seasonal cyclicity in sea surface temperatures recorded in the $\delta^{18}\text{O}_c$
78 of corals and mollusks and seasonal cyclicity in the $\delta^{18}\text{O}_w$ of precipitation recorded in speleothems
79 (Dunbar and Wellington, 1981; Schöne et al., 2005; Van Rampelbergh et al., 2014). This relationship is
80 challenged in tropical latitudes, where temperature seasonality is restricted. However, in some tropical
81 archives, the annual cycle of $\delta^{18}\text{O}_w$ in precipitation still allows the annual cycle to be resolved from $\delta^{18}\text{O}$
82 records (e.g. Evans and Schrag, 2004). These properties make $\delta^{18}\text{O}_c$ one of the most highly sought-
83 after proxies for climate variability, and high-resolution $\delta^{18}\text{O}_c$ records are abundant in the paleoclimate
84 literature (e.g. Lachnit, 2009; Lough, 2010; Schöne and Gillikin, 2013 and references therein).

85 The close relationship between $\delta^{18}\text{O}_c$ records and the seasonal cycle can also be exploited to estimate
86 variability in growth rate of the archive. This property of $\delta^{18}\text{O}_c$ curves has been recognized by previous

87 authors, and attempts have been made to quantify intra-annual growth rates from the shape of $\delta^{18}\text{O}_c$
88 profiles (Wilkinson and Ivany, 2002; Goodwin et al., 2003; De Ridder et al., 2006; Goodwin et al., 2009;
89 De Brauwere et al., 2009; Müller et al., 2015; Judd et al., 2018). Over time, these so called "growth
90 models" have improved from fitting of sinusoids to $\delta^{18}\text{O}_c$ data (Wilkinson and Ivany, 2002; De Ridder et
91 al., 2006) to including increasingly complicated (inter)annual growth rate curves to the model to fit the
92 shape of the $\delta^{18}\text{O}_c$ data (Goodwin et al., 2003; 2009; Müller et al., 2015; Judd et al., 2018). These later
93 models manage to fit the shape of $\delta^{18}\text{O}_c$ records well, but they often rely on detailed *a priori* knowledge
94 of growth rate or temperature patterns (e.g. Goodwin et al., 2003; 2009), which requires measurements
95 of one or more parameters in the environment. These measurements are not available in studies on
96 carbonate archives from the archeological or geological past. In contrast, the latest model by Judd et al.
97 (2018; [GRATAISS, or "Growth Rate and Temporal Alignment of Isotopic Serial Samples"](#)) is based only
98 on the assumption that growth and temperature follow quasi-sinusoidal patterns and can therefore work
99 with $\delta^{18}\text{O}_c$ data alone, making it more widely applicable. The simplified parameterization of temperature
100 and growth rate seasonality by Judd et al. (2018) using two (skewed) sinusoids is demonstrated to
101 approximate natural circumstances very well.

102 However, the [approach by Judd et al. \(2018\)GRATAISS model](#) is still limited in its use, because it
103 requires whole, individual growth years to be analyzed separately, resulting in a discontinuous time
104 series when applied on records containing multiple years of $\delta^{18}\text{O}_c$ data and no solution for incomplete
105 years. In addition, the model has no option to supply information about the less dominant factor that
106 drives $\delta^{18}\text{O}_c$ values ($\delta^{18}\text{O}_w$ of sea water in the case of mollusks and corals). Furthermore, only estimates
107 from aragonite records are supported, while the [\$\delta^{18}\text{O}_c\$ value of the](#) other dominant carbonate mineral,
108 calcite, has a different temperature relationship (Kim and O'Neil, 1997). Finally, neither of the models
109 highlighted above except for the MoGroFun model by Goodwin et al. (2009) include any assessment of
110 the uncertainty of the constructed age model.

111 Here, a new model for estimating ages of samples in seasonal $\delta^{18}\text{O}_c$ curves is presented which
112 combines the advantages of previous models while attempting to negate their disadvantages.
113 ShellChron combines a skewed growth rate sinusoid with a sinusoidal temperature curve to model $\delta^{18}\text{O}_c$
114 using the Shuffled Complex Evolution model developed at the University of Arizona (SCEUA; Duan et
115 al., 1992; following Judd et al., 2018). It applies this optimization using a sliding window through the
116 dataset (as in Wilkinson and Ivany, 2002) and includes the option to use a Monte Carlo simulation

117 approach to combine uncertainties on the input ($\delta^{18}\text{O}_c$ and sample distance measurements) and the
118 model routine (as in Goodwin et al., 2009). As a result, ShellChron produces a continuous time series
119 with a confidence envelope, supports records from multiple carbonate minerals and allows the user to
120 provide information on the less dominant variable influencing $\delta^{18}\text{O}_c$ (e.g. $\delta^{18}\text{O}_w$) if available (see **section**
121 **2**). The modular design of ShellChron's functional script allows parts of the model to be adapted and
122 interchanged, supporting a wide range of climate and environmental archives. As a result, the initial
123 design of ShellChron for reconstructing age models in temperature-dominated $\delta^{18}\text{O}_c$ records from
124 marine bio-archives (e.g. corals and mollusks) presented here can be easily modified for application on
125 other types of records. The routine is worked out into a ready-to-use package for the open-source
126 computational programming language R and is directly available without restrictions, allowing all
127 interested parties to freely modify and build on the base structure to adapt it to their needs (R Core
128 Team, 2020; full package code and documentation in **SI1**, see also **Code availability**).

129

130 **2. Scientific basis**

131 The relationship between $\delta^{18}\text{O}_c$ and the temperature of carbonate precipitation was first established by
132 Urey (1951) and later refined with additional measurements and theoretical models (e.g. Epstein et al.,
133 1953; Tarutani et al., 1969; Grossman and Ku, 1986; Kim and O'Neil, 1997; Coplen, 2007; Watkins et
134 al., 2014; Daëron et al., 2019). Empirical transfer functions for aragonite and calcite by Grossmann and
135 Ku (1986; modified by Dettmann et al., 1999; **equation 1**) and Kim and O'Neil (1997; **equation 2**, with
136 VSMOW to VPDB scale conversion following Brand et al., 2014; **equation 3**) have so far found most
137 frequent use in modern paleoclimate studies and are therefore applied as default relationships in the
138 ShellChron model (see *d18O_model* function).

139
$$T[\text{°C}] = 20.6 - 4.34 * (\delta^{18}\text{O}_c[\text{‰VPDB}] - \delta^{18}\text{O}_w[\text{‰VSMOW}] + 0.2) \quad (1)$$

140
$$1000 * \ln(\alpha) = 18.03 * \frac{10^3}{(T[\text{°C}] + 273.15)} - 32.42$$

141
$$\text{with } \alpha = \frac{\left(\frac{\delta^{18}\text{O}_c[\text{‰VPDB}]}{1000} + 1\right)}{\left(\frac{\delta^{18}\text{O}_w[\text{‰VPDB}]}{1000} + 1\right)} \quad (2)$$

142
$$\delta^{18}\text{O}_w[\text{‰VPDB}] = 0.97002 * \delta^{18}\text{O}_w[\text{‰VSMOW}] - 29.98 \quad (3)$$

143 To apply these formulae, it is assumed that carbonate is precipitated in equilibrium with the precipitation
144 fluid. Which carbonates are precipitated in equilibrium has long been subject to debate, and the
145 development of new techniques for measuring the carbonate-water system (e.g. clumped and dual-
146 clumped isotope analyses; Daëron et al., 2019; Bajnai et al., 2020) has led **recent-some** authors to
147 challenge the assumption that equilibrium fractionation is the norm (see **Supplementary Discussion**).
148 The modular character of ShellChron allows the empirical transfer function to be adapted to the $\delta^{18}\text{O}_c$
149 record or to the user's preference for alternative transfer functions by a small modification of the
150 *d18O_model* function. Future versions of the model will include more options for changing the transfer
151 function (see **Model description**).

152 As the name suggests, the ShellChron model was initially developed for application on $\delta^{18}\text{O}_c$ records
153 from marine calcifiers (e.g. mollusk shells and corals). ShellChron approximates the evolution of the
154 calcification temperature at which the carbonate is precipitated by a sinusoidal function (see **equation**
155 **4**, **Table 1** and **SI4**; *temperature_curve* function; visualized in **Fig. 4A** and **Fig S1**), a good approximation
156 of seasonal temperature fluctuations in most marine and terrestrial environments (Wilkinson and Ivany,
157 2002; [Ivany and Judd, 2022](#)). Variability in $\delta^{18}\text{O}_w$ is also comparatively limited in most marine
158 environments (except for regions with sea ice formation), making the model easy to use in these settings
159 (LeGrande and Schmidt, 2006; Rohling, 2013). Nevertheless, ShellChron includes the option to provide
160 *a priori* knowledge about $\delta^{18}\text{O}_w$, ranging from annual average values to detailed seasonal variability,
161 enabling the model to work in environments with more complex interaction between $\delta^{18}\text{O}_w$ and
162 temperature on the $\delta^{18}\text{O}_c$ record (see **equations 1 and 2**). This $\delta^{18}\text{O}_w$ data can be provided either as a
163 vector (with the same length as the data) or a single value (assuming constant $\delta^{18}\text{O}_w$) through the *d18Ow*
164 parameter in the *run_model* function.

$$165 T[^\circ\text{C}] = T_{av} + \frac{T_{amp}}{2} \sin\left(\frac{2\pi * (t[d] - T_{pha} + \frac{T_{per}}{4})}{T_{per}}\right) \quad (4)$$

166

Table 1: Overview of model parameters

Name	Description	Unit	Range
T_{av}	Average temperature	°C	Variable, generally between 0°C–30°C
T_{amp}	Temperature range (2*amplitude)	°C	Variable, generally <20°C
T_{pha}	Phase of temperature sinusoid	d	0–365 days
T_{per}	Period of temperature sinusoid	d	365 days by default
G_{av}	Average growth rate	µm/d	Variable, generally between 0–100 µm/day
G_{amp}	Range of growth rates	µm/d	Variable, generally <200 µm/day
G_{pha}	Phase of growth rate sinusoid	d	0–365 days
G_{per}	Period of growth rate sinusoid	d	365 days by default
G_{skw}	Skewness factor of GR sinusoid	-	0–100, with 50 meaning no skew
D	Distance along the record	µm	Depends on archive
t	Age	d	Depends on archive
L_{win}	Length of sampling window	#	Depends on sampling resolution
w	Weighting factor on sample	-	0–1
i	Position relative to model window	-	0– L_i
I	Intercept of sinusoid (T_{av} or G_{av})	°C or µm/d	
A	Amplitude of sinusoid ($\frac{T_{amp}}{2}$ or $\frac{G_{amp}}{2}$)	°C or µm/d	
P	Period of sinusoid (T_{per} or G_{per})	d	
φ	Phase of sinusoid (T_{pha} or G_{pha})	d	

167

168 If marine $\delta^{18}\text{O}_c$ records represent one extreme on the spectrum of temperature versus $\delta^{18}\text{O}_w$ influence
 169 on the $\delta^{18}\text{O}_c$ record, cave environments, in which $\delta^{18}\text{O}_c$ variability is predominantly driven by $\delta^{18}\text{O}_w$
 170 variability in the precipitation fluid, represent the other extreme (Van Rappelbergh et al., 2014). In its
 171 current form, ShellChron takes $\delta^{18}\text{O}_w$ as a user-supplied parameter to model temperature and growth
 172 rate variability, but future versions will allow temperature to be fixed, while $\delta^{18}\text{O}_w$ becomes the modelled
 173 variable. ShellChron's modular character makes it possible to implement this update without changing
 174 the structure of the model. Application of ShellChron on $\delta^{18}\text{O}_c$ records from cave deposits will have to
 175 be treated with caution, since drip water $\delta^{18}\text{O}_w$ seasonality (if present) cannot always be approximated
 176 by a sinusoidal function and equilibrium fractionation in cave deposits is less common than in bio-
 177 archives (Baldini et al., 2008; Daeron et al., 2011; Van Rappelbergh et al., 2014).

178 Besides temperature (or $\delta^{18}\text{O}_w$) seasonality, ShellChron models the growth rate of the archive to
 179 approximate the $\delta^{18}\text{O}_c$ record (see **equation 5**, **Table 1** and **SI4**; *growth_rate_curve* function; visualized
 180 in **Fig. 4B** and **Fig S2**). Since the growth rate in many carbonate archives varies seasonally, a quasi-
 181 sinusoidal model for growth rate seems plausible (e.g. Le Tissier et al., 1994; Baldini et al., 2008; Judd
 182 et al., 2018). However, as discussed in Judd et al. (2018), the occurrence of growth cessations (growth
 183 rate = 0) and skewness in seasonal growth patterns calls for a more complex growth rate model that

184 can take these properties into account. Therefore, ShellChron uses a slightly modified version of the
 185 skewed sinusoidal growth function described by Judd et al. (2018; **equation 5**). Note that the added
 186 complexity of this function does not preclude the modelling of growth rate functions described by a
 187 simple sinusoid (no skewness; $G_{skw} = 50$) or even constant growth through the year ($G_{amp} = 0$; see **Table**
 188 **1**).

$$189 G[\text{mm/yr}] = G_{av} + \frac{G_{amp}}{2} \sin\left(\frac{2\pi * (t[d] - G_{pha} + G_{per} * S)}{P}\right)$$

$$190 \text{with } S = \begin{cases} \frac{100 - G_{skw}}{50}, & \text{if } t[d] - G_{pha} < G_{per} \frac{100 - G_{skw}}{100} \\ \frac{G_{skw}}{50}, & \text{if } t[d] - G_{pha} \geq G_{per} \frac{100 - G_{skw}}{100} \end{cases} \quad (5)$$

191 Contrary to previous $\delta^{18}\text{O}_c$ growth models, ShellChron allows uncertainties on the input variables
 192 (sampling distance and $\delta^{18}\text{O}_c$ measurements) as well as uncertainties of the full modelling approach to
 193 be propagated, providing confidence envelopes around the chronology. Uncertainty propagation is
 194 optional and can be skipped without compromising model accuracy. Standard deviations of uncertainties
 195 on input variables (sampling distance and $\delta^{18}\text{O}_c$) can be provided by the user, while model uncertainties
 196 are calculated from the variability in model results of the same datapoint obtained from overlapping
 197 simulation windows (see *growth_model* function). Measurement errors are combined by projecting
 198 Monte Carlo simulated values for sampling distance and $\delta^{18}\text{O}_c$ measurements on the modelled $\delta^{18}\text{O}_c$
 199 curve through an orthogonal projection (**equation 6**; *mc_err_orth* function; visualized in **Fig S3**). The
 200 measurement uncertainty projected on the distance domain is then combined with the model uncertainty
 201 to obtain pooled uncertainties in the distance domain, which are propagated through the modelled $\delta^{18}\text{O}_c$
 202 record to obtain uncertainties on the model result in the age domain. As a result of the sliding window
 203 approach in ShellChron, model results for datapoints situated at the edges of windows are more
 204 sensitive to small changes in the modelled parameters and therefore possess a larger model
 205 uncertainty. To prevent these least certain model estimates from affecting the stability of the model,
 206 model results are given more weight the closer they are situated towards the center of the model window
 207 (see **equation 7** in *export_results* function; see also **Fig. S4**). This weighting is also incorporated in
 208 uncertainty propagation through a weighted standard deviation (see **equation 8** from the *sd_wt*
 209 function). Note that, despite the weighting solution, the size of uncertainties on the first and last positions

210 in the $\delta^{18}\text{O}_c$ record remains uncertain since they are based on a smaller number of overlapping windows
211 (see e.g. [Figure 3](#)).

212

$$\sigma_{meas} = \sqrt{\left(\frac{D_{sim} - \bar{D}_{sim}}{\sigma_D}\right)^2 + \left(\frac{\delta^{18}O_{sim} - \bar{\delta}^{18}O_{sim}}{\sigma_{\delta^{18}O}}\right)^2} \quad (6)$$

213

$$w[i] = 1 - \left| \frac{2i}{L_{window}} - 1 \right| \quad (7)$$

214

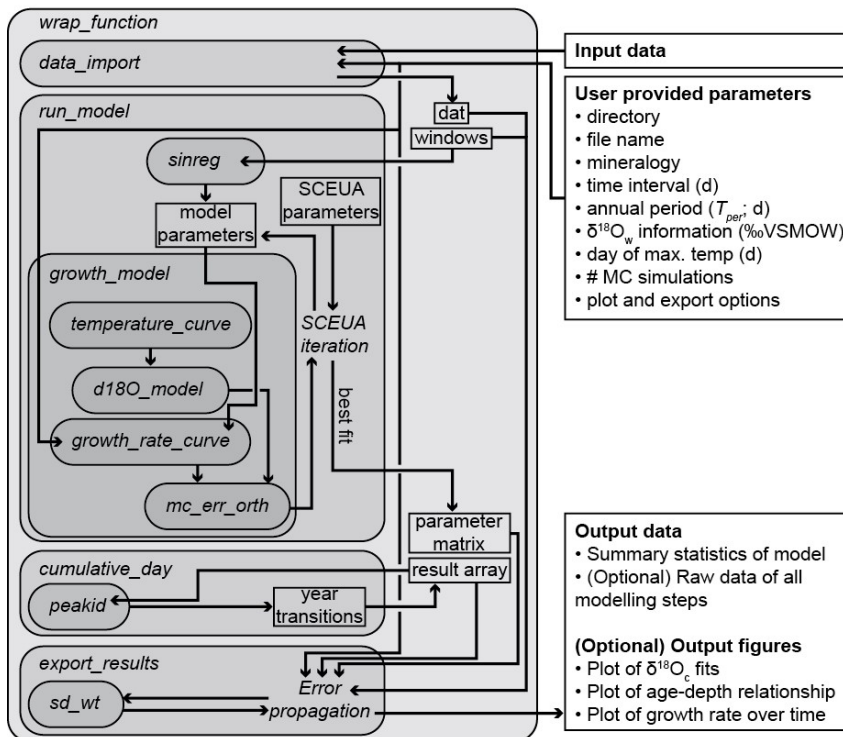
$$\sigma_{weighted,i} = \sqrt{\frac{w_i * (x_i - \bar{w})^2}{\sum w[i] * \frac{N-1}{N}}} \quad (8)$$

215

216 **3. Model description**

217 ShellChron is organized [in-as](#) a series of functions that describe the step-by-step modelling process. A
218 schematic overview of the model is given in [Fig. 1](#). A short **Test Case** is used to illustrate the modelling
219 steps in ShellChron. [Fig. 2](#) shows how the virtual **Test Case** was created from randomly generated
220 seasonal growth rate, $\delta^{18}\text{O}_w$ and temperature curves using the *seasonal/clumped* R package (de Winter
221 et al., 2021a; see [Fig. 2, Supplementary Methods](#) and [SI2](#)) A wrapper function (*wrap_function*) is
222 included, which carries out all steps of the model procedure in succession to promote ease of use.

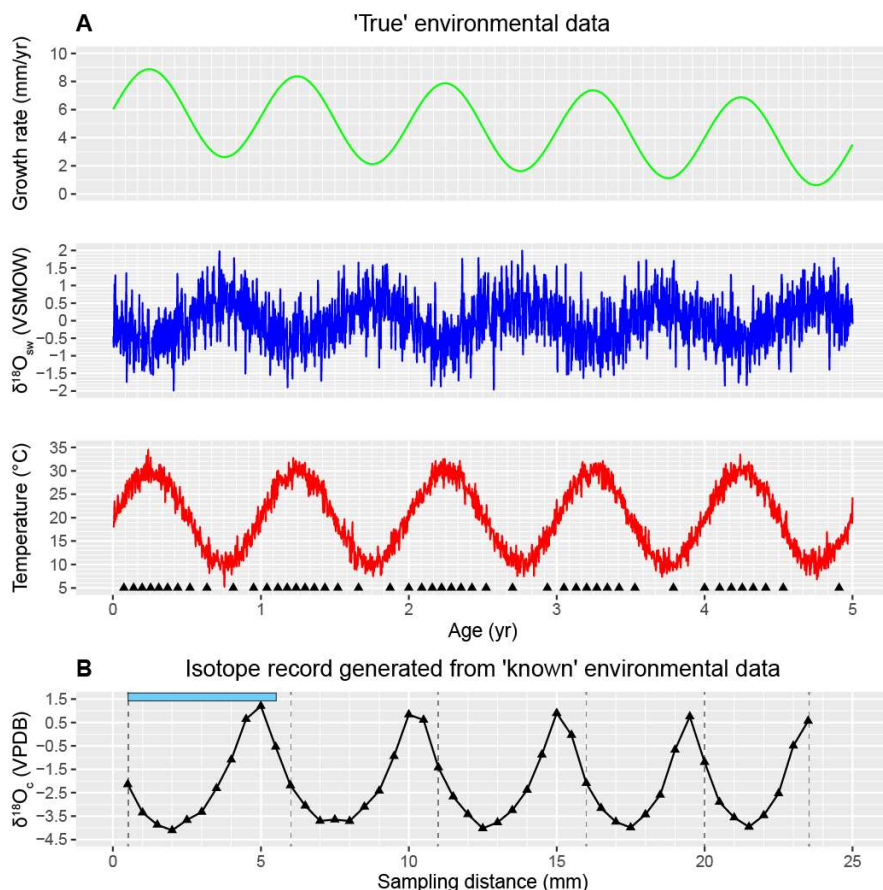
Schematic overview of ShellChron model



224

225 **Figure 1:** Schematic overview of ShellChron. Names in *italics* refer to functions (encapsulated in
 226 rounded rectangular boxes) and operations within functions. Rectangular boxes represent data. Arrows
 227 represent the flow of information between model components. Note that some operations are
 228 encapsulated in functions (e.g. *Error propagation* in *export results*) and that some functions are only
 229 used within other functions (e.g. *peakid* in *cumulative_day*). All data structures outside *wrap_function*
 230 represent input and output of the model. Detailed documentation of all functions and operations in
 231 ShellChron is provided in **SI1** (see also **Code availability**).

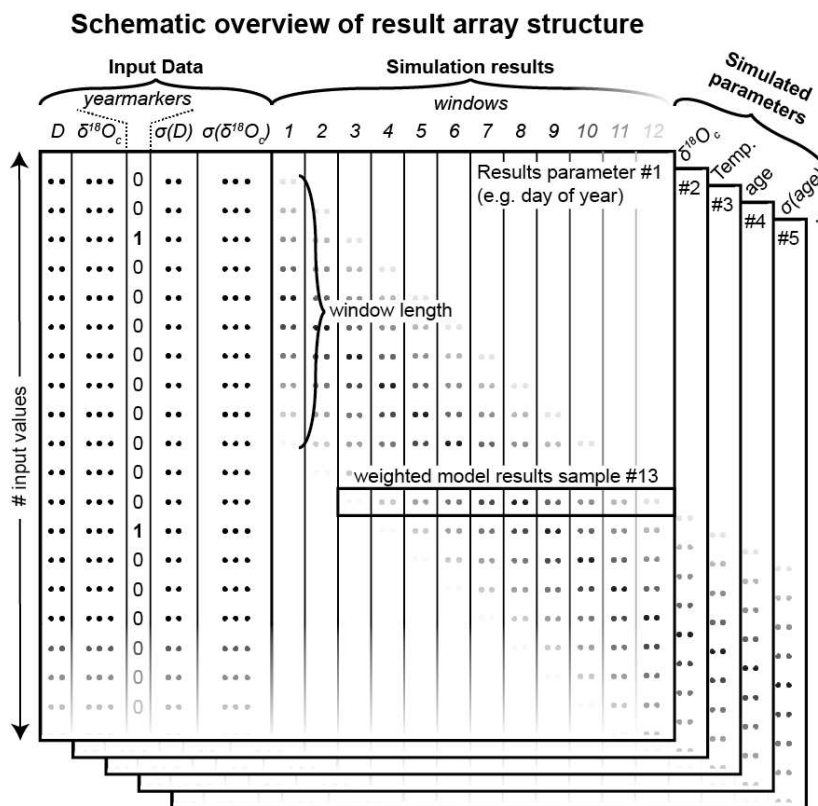
232



233
234 **Figure 2: A)** Plots of the growth rate (light green), $\delta^{18}\text{O}_{\text{w}}$ (blue) and tT emperature (red) records (in time
235 domain) from which the **Test case** was produced. Black triangles on the bottom of the temperature
236 plot indicate the ages of the samples taken from the record. **B)** The $\delta^{18}\text{O}_{\text{c}}$ record for the **Test Case**
237 generated after equidistant sampling using the *seasonalclumped* package (de Winter et al., 2021a)
238 with a sampling interval of 0.5 mm. Error bars on sampling distance (0.1 mm) and $\delta^{18}\text{O}_{\text{c}}$ (0.1‰) fall
239 within the symbols. Vertical grey dashed lines indicate user-provided year markers and the blue bar on
240 top of this plot shows an example of the width of a modelling window. See **Supplementary Methods**
241 for details on producing the **Test case** $\delta^{18}\text{O}_{\text{c}}$ record and **SI3** for the R script used to generate the data.

242 Data is imported through the `data_import` function, which takes a comma-separated text file (CSV) with
243 the input data. Data files need to contain columns containing sampling distance (D , in μm) and $\delta^{18}\text{O}_c$
244 data (in ‰VPDB), a column marking years in the record (`yearmarkers`) and two optional columns
245 containing uncertainties on sampling distance ($\sigma(D)$, one standard deviation, in μm) and $\delta^{18}\text{O}_c$ ($\sigma(\delta^{18}\text{O}_c)$,
246 one standard deviation, in ‰) respectively (see example in **SI2** and **Figure 3**). The function uses the
247 year markers (third column) as guidelines for defining the minimum length of the model windows to
248 ensure that all windows contain at least one year of growth. **Window sizes are defined to contain at least**
249 **two year markers (see Fig. 2)**—By default, consecutive windows are shifted by one datapoint, yielding a
250 total number of windows equal to the sample size minus the length of the last window. While year
251 markers are required for ShellChron to run (otherwise no windows can be defined), the result of the
252 model does not otherwise depend on user-provided year markers, instead basing the age result purely
253 on simulations of the $\delta^{18}\text{O}_c$ data.

254



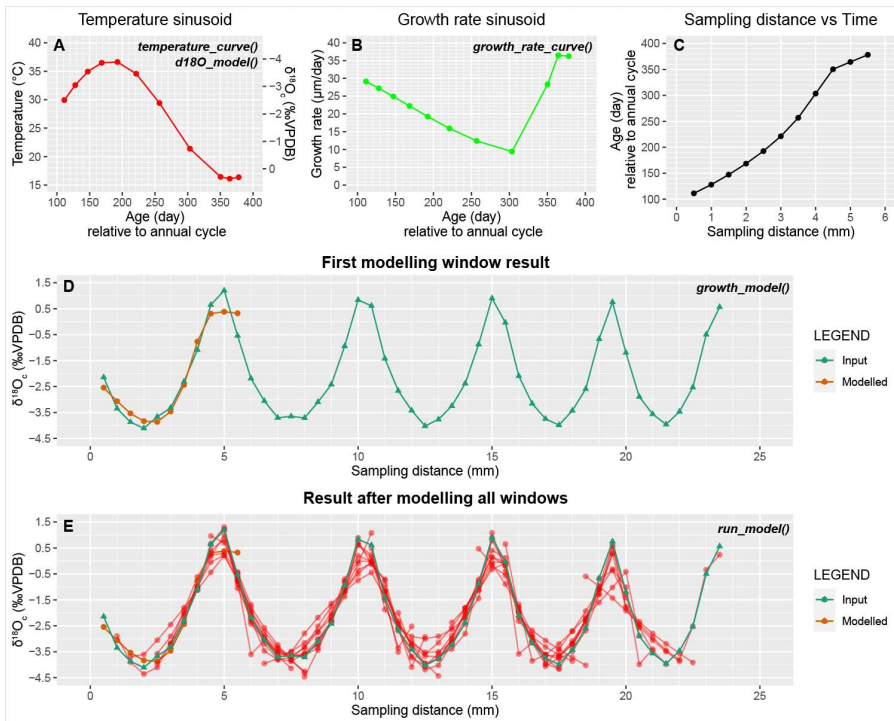
255

256 **Figure 3:** Schematic overview of the structure of the result array in which ShellChron stores the raw
 257 results of each model window. Data is stored in three dimensions: The sample number (rows in the
 258 figure), the window number (columns in the figure) and the number of modelled parameters
 259 (represented by the stacked table “sheets” in the figure). Note that the first 5 columns of each “sheet”
 260 represent the user-provided input data (see example in **SI2**), and that the model result data starts from
 261 column 6. The window length is determined by the user-provided indication of year transitions (column
 262 3). Rows of dots in the figure are placeholders for (input or result) values. Shading of these dots in the
 263 window columns indicate differential **weighing** of modelled values in function of their location
 264 relative to the sliding window. The horizontal box shows how these **weighing** factors within
 265 each sample window (in vertical direction) result in **weighing** of different estimates of
 266 modelled parameters for the same data point (in horizontal direction). Shading of input data and
 267 window number towards the bottom and right edge of the figure, respectively, indicates that the

268 number of input values (and thus simulation windows) is only limited to the length of the input table
269 and may therefore continue indefinitely (at the expense of longer computation times, see **Fig. 8** in
270 **Model performance**).

271 The core of the model consists of simulations of overlapping subsamples (windows) of the sampling
272 distance and $\delta^{18}\text{O}_c$ data described by the *run_model* function (see **Fig. 1 and 3**). Data and window sizes
273 are passed from *data_import* onto *run_model* along with user-provided parameters (e.g. $\delta^{18}\text{O}_w$
274 information; see **Fig. 1**). *run_model* loops through the data windows and calls the *growth_model*
275 function, which fits a modelled $\delta^{18}\text{O}_c$ vs. distance curve through the data using the SCEUA optimization
276 algorithm (see Duan et al., 1992; see example in **Fig 4**). The simulated $\delta^{18}\text{O}_c$ curve is produced through
277 a combination of a temperature sinusoid (*temperature_curve* function; see **equation 4**, **Fig. 4A** and **Fig.**
278 **S1**) and a skewed growth rate sinusoid (*growth_rate_curve*; see **equation 5**, **Fig. 4B** and **Fig. S2**), with
279 temperature data converted to $\delta^{18}\text{O}_c$ data through the *d18O_model* function (**equation 1 and 2**; **Fig.**
280 **4A**).

281



282

283 **Figure 4:** Showing the steps taken to simulate $\delta^{18}\text{O}_c$ data in the `run_model()` function on the **Test case**.
 284 **A)** Temperature sinusoid used to approximate $\delta^{18}\text{O}_c$ data in the first modelling window (see **D**), produced
 285 using a combination of `temperature_curve` and `d18O_model` functions. Symbols indicate the positions
 286 of $\delta^{18}\text{O}_c$ samples on the temperature curve, with estimated $\delta^{18}\text{O}_c$ values shown on the secondary axis
 287 (right). **B)** Skewed growth rate sinusoid fit to the $\delta^{18}\text{O}_c$ data using the `growth_rate_curve` function. Note
 288 the shift towards steeper growth rate increase around the 300th model day (autumn season in this
 289 example). See **Fig. S2** for a detailed description of the growth rate sinusoid. **C)** The modelled age-
 290 distance relationship for this window after fitting $\delta^{18}\text{O}_c$ data, resulting from aligning the estimated age of
 291 samples (x-axes on **A**) with the distance in sampling direction (x-axis in **D**) using the cumulative growth
 292 rate function (**B**). **D)** $\delta^{18}\text{O}_c$ profile of the **Test case** (green) with the $\delta^{18}\text{O}_c$ curve of the first modelling
 293 window (red), which results from the combination of temperature (**A**) and growth rate (**B**) sinusoids,
 294 plotted on top (`growth_model` function). **E)** Result after simulating the full $\delta^{18}\text{O}_c$ profile of the **Test case**
 295 (green) using `run_model`, with the $\delta^{18}\text{O}_c$ curves of individual modelling windows shown in red.

296 By default, starting values for the parameters describing temperature and growth rate curves are
 297 obtained by estimating the annual period (P) through a spectral density estimation and applying a
 298 linearized sinusoidal regression through the $\delta^{18}\text{O}_c$ data (*sinreg* function; see **equation 9**). It is possible
 299 to skip this sinusoidal modelling step through the “*sinfit*” parameter in the *run_model* function, in which
 300 case the starting value for the annual period is set equal to the width of the model window. In addition,
 301 *growth_model* takes a series of parameters describing the method for SCEUA optimization (see Duan
 302 et al., 1992; Judd et al., 2018) and the upper and lower bounds for parameters describing temperature
 303 and growth rate curves (see **SI4**). Parameters for the SCEUA algorithm (*iniflg*, *ngs*, *maxn*, *kstop*, *pcento*
 304 and *peps*) in the *run_model* function may be modified by the user to reach more desirable optimization
 305 outcomes. The effect of changing the SCEUA parameters on the model result for the **Test case** is
 306 illustrated in **section 4.1** (see **Fig. 5**). If uncertainties on sampling distance and $\delta^{18}\text{O}_c$ data are provided,
 307 *growth_model* calls the *mc_err_orth* function to propagate these errors through the model result (see
 308 **equation 6** and **Fig S3**).

$$309 \delta^{18}\text{O}_c[\text{\%oVPDB}] = I + \frac{A}{2} \sin \left(\frac{2\pi * (D - \varphi + \frac{P}{4})}{P} \right),$$

$$310 \text{linearized as: } \delta^{18}\text{O}_c[\text{\%oVPDB}] = a + b \sin \left(\frac{2\pi}{P} * D \right) + c \cos \left(\frac{2\pi}{P} * D \right),$$

$$311 \text{with } I = a; A = \sqrt{b^2 + c^2} \text{ and } \varphi = P * \left(0.25 - \frac{\cos^{-1}(\frac{b}{A})}{2\pi} \right) \quad (9)$$

312 The *run_model* function returns an array listing day of the year (1–365), temperature, $\delta^{18}\text{O}_c$, growth rate
 313 and (optionally) their uncertainty standard deviations as propagated from uncertainties on the input data
 314 (“result array”; see **Fig. 3** and **SI5**). Note that the default length of the year (*Tper* and *Gper*) is set at 365
 315 days, but that these parameters can be modified by the user in *run_model*. In addition, a matrix
 316 containing the optimized parameters of temperature and growth rate curves is provided, yielding
 317 information about the evolution of mean values, phases, amplitudes, and skewness of seasonality in
 318 temperature and growth rate along the record (“parameter matrix”, see **Fig. 1** and **SI6**). To construct an
 319 age model for the entire record, the modelled timing of growth data, expressed as day relative to the
 320 365-day year, is converted into a cumulative time series listing the number of days relative to the start
 321 of the first year represented in the record (rather than relative to the start of the year in which the

322 datapoint is found). This requires year transitions (transitions from day 365 to day 1) to be recognized
323 in all the model results. The *cumulative_day* function achieves this by aggregating information about
324 places where the beginning and end of the year is recorded in individual window simulations and
325 applying a peak identification algorithm (*peakid* function) to find places in the record where year
326 transitions occur (see **Supplementary Methods**). Results of the timing of growth for each sample (in
327 day of the year) are converted to a cumulative time scale using their positions relative to these
328 recognized year transitions (**Supplementary Methods**).

329 In a final step (described by the *export_results* function), the results from overlapping individual
330 modelling windows are combined to obtain mean values and 95% confidence envelopes of the result
331 variables (age, $\delta^{18}\text{O}_c$, $\delta^{18}\text{O}_c$ -based temperatures and growth rates) for each sample in the input data. If
332 uncertainties on the input variables were provided, these are combined with uncertainties on the
333 modelling result calculated from results of the same datapoint on overlapping data windows by pooling
334 the variance of the uncertainties (**equation 10**). Throughout this merging of data from overlapping
335 windows, results from datapoints on the edge of windows are given less weight than those from
336 datapoints near the center of a window (see **equation 7** and **Fig. S4**). This weighting procedure
337 corrects for the fact that datapoints near the edge of a window are more susceptible to small changes
338 in the model parameters and are therefore less reliable than results in the center of the window. Finally,
339 summaries of the simulation results and the model parameters including their confidence intervals are
340 exported as comma-separated (CSV) files. In addition, *export_results* supports optional exports of
341 figures displaying the model results and files containing raw data of all individual model windows
342 (equivalent to "sheets" of the result array, see **Fig. 3** and **SI5**).

$$VAR_{pooled} = \frac{\sum_i((N_i-1)*VAR_i*w_i)}{\sum_i(N_i)-n} \quad (10)$$

344 in which w = weight of the individual reconstructions, N is the sample size and n is the number of
345 reconstructions (indexed by i) that is combined

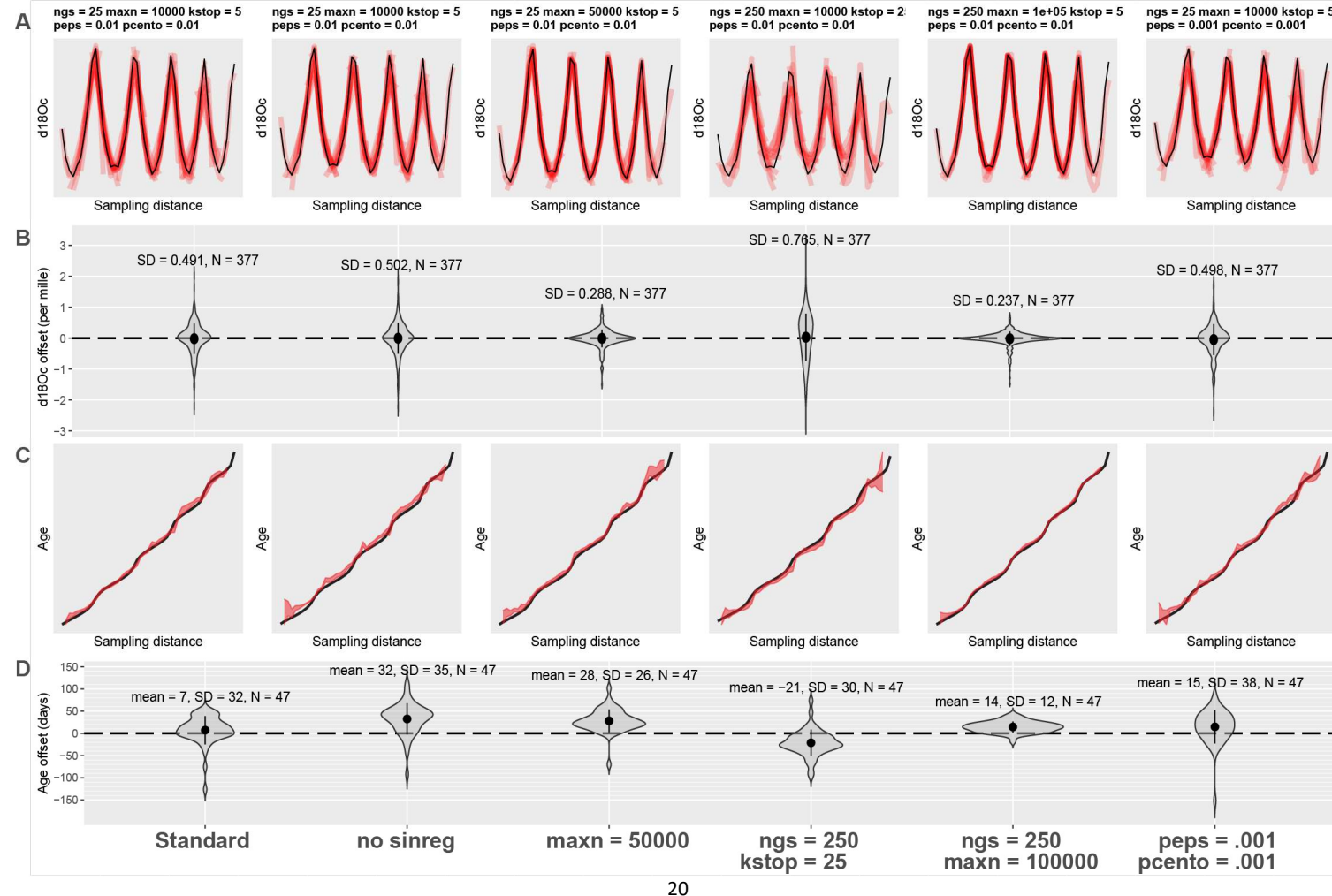
346

347 **4. Model performance**

348 The performance of ShellChron was first tested on three virtual datasets:

349 1. The short **Test case** used to illustrate the model steps above (see **Fig. 2 and 4; SI7**)
350 2. A $\delta^{18}\text{O}_c$ record constructed from a simulated temperature sinusoid with added stochastic noise
351 (**Case 1; SI8**)
352 3. A record based on a real-known high-resolution sea surface temperature and salinity record
353 measured on the coast of Texel island in the tidal basin of the Wadden Sea (North Netherlands;
354 **Texel**, see details in **SI9** and de Winter et al., 2021a and **Supplementary Methods**).

355 Firstly, the effect of varying parameters in the SCEUA algorithm is tested on the **Test Case (Fig. 5)**.
356 Then, full model runs on **Case 1** and **Texel** are evaluated in terms of model performance (**Fig. 6**).
357 In addition to the three test cases, three modern carbonate $\delta^{18}\text{O}_c$ records were internally dated using
358 ShellChron (see **Fig. 7**): a tropical stony coral (*Porites lutea*; hereafter: **coral**) from the Pandora
359 Reef (Great barrier Reef, NE Australia; Gagan et al., 1993; see **SI10**), a Pacific oyster shell
360 (*Crassostrea gigas*; hereafter: **oyster**) from List Basin in Denmark (Ullmann et al., 2010; see **SI10**)
361 and a temperate zone speleothem from Han-sur-Lesse cave (Belgium; hereafter: **speleothem**; see
362 Vansteenberghe et al., 2019; see **SI10**). Finally, ShellChron's performance in terms of computation
363 time and accuracy is compared to that of the most comprehensive pre-existing $\delta^{18}\text{O}_c$ -based age
364 model (GRATAISS model by Judd et al., 2018) on simulated temperature sinusoids of various
365 length and sampling resolutions to which stochastic noise was added (*sensu Case 1*; de Winter et
366 al., 2021a; see **Fig. 8 and SI11**). The latter also demonstrates the scalability of ShellChron and its
367 application on a variety of datasets. Timing comparisons were carried out using a modern laptop
368 (Dell XPS13-7390; Dell Inc., Round Rock, Tx, USA) with an Intel Core i7 processor (8 MB cache,
369 4.1 GHz clock speed, 4 cores, Intel Corporation, Santa Clara, CA, USA), 16 GB LPDDR3 RAM and
370 aan SSD drive running Windows 10. Note that ShellChron was built and tested successfully on Mac
371 OS, Fedora Linux and Ubuntu Linux as well.



373 **Figure 5:** Result of testing ShellChron with various combinations of SCEUA parameters and
374 sinusoidal regression on the **Test case** dataset (see **Fig. 2**). The leftmost plots illustrate performance
375 of ShellChron under default SCEUA parameters. Plots to the right show various combinations of
376 parameters that deviate from the default (see labels on top and bottom of plot) **A**) Fits of the model
377 $\delta^{18}\text{O}_c$ curves (red) with the data (black). **B**) Violin plots showing the distribution of modelled $\delta^{18}\text{O}_c$
378 offset from the data. **C**) Age-distance plots showing modelled (red) and true-known (black) age-depth
379 relationships for each scenario. **D**) Violin plots showing the distribution of age offsets from the real
380 known age-depth relationship. SD = standard deviation, N = number of datapoints, sinres = sinusoidal
381 regression, maxn, ngs, kstop, peps and pcento are SCEUA parameters (see Duan et al., 1992 and
382 explanation in **section 4.1**). Data on test results is provided in **SI11**.

383 **4.1 Testing model parameters**

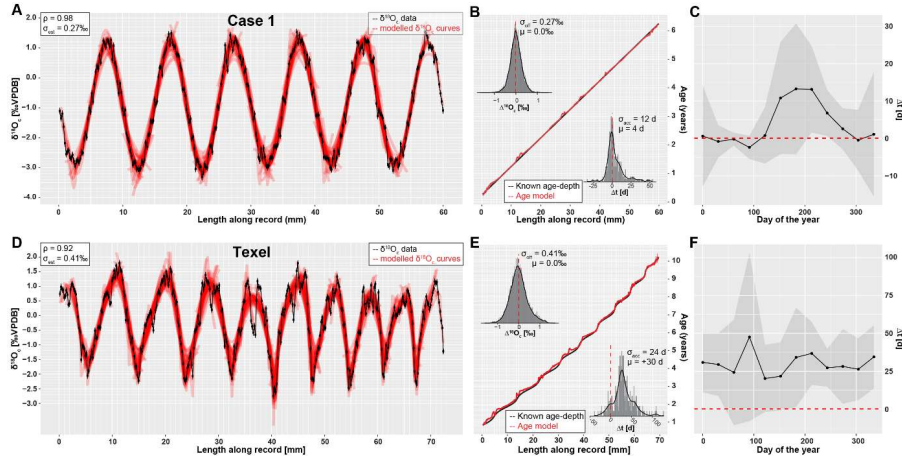
384 Testing different combinations of modelling parameters (**Fig. 5**) shows that, while the results of
385 ShellChron can improve beyond the default SCEUA parameters and sinusoidal regression, care must
386 be taken to evaluate the effect of changing modelling parameters on both the $\delta^{18}\text{O}_c$ fit and the age-
387 distance relationship. Comparative testing on the **Test case** (**Fig. 5**) shows that sinusoidal regression
388 has a negligible influence on the success of ShellChron fitting the $\delta^{18}\text{O}_c$ curve (**Fig. 5A-B**; standard
389 deviation on $\delta^{18}\text{O}_c$ is 0.49‰ with sinusoidal regression and 0.50‰ without). However, ShellChron with
390 sinusoidal regression performs better in terms of age approximation, with a mean age offset of only 7
391 ± 32 days with sinusoidal regression against 32 ± 35 days without (**Fig. 5C-D**). Age-distance plots
392 (**Fig. 5C**) show that the model without sinusoidal fit shows a phase offset with respect to the real
393 known age-depth-distance relationship, resulting in overestimation of the age for much of the record.
394 Sinusoidal regression probably results in better initial parameter estimation, which helps to avoid
395 phase offsets like the one shown in **Fig. 5**. For the remainder of the tests, sinusoidal regression was
396 usedenabled.

397 The remainder of the tests show that the main bottleneck towards better $\delta^{18}\text{O}_c$ fit optimization is the
398 maximum number of function evaluations allowed within a single modelling cycle (maxn; see **Fig. 5**).
399 Increasing the other SCEUA parameters, such as the number of complexes in the SCEUA routine
400 (ngs), the number of shuffling loops that should show a significant change before convergence (kstop)
401 and the thresholds for significant change in parameter value (peps) or result value (pcento) does not

402 improve the result if the SCEUA algorithm is not allowed more processing time (maxn). In fact, **Fig. 5**
403 shows that increasing these SCEUA parameters can actually result in a worse deterioration of the
404 $\delta^{18}\text{O}_c$ fit and higher uncertainty on the age result (**Fig. 5B and D**). A fivefold increase in maxn (maxn =
405 50000) almost halves the standard deviation on $\delta^{18}\text{O}_c$ residuals (from 0.49‰ to 0.29‰; **Fig. 5B**) and
406 decreases the standard deviation on the age model offset from 32 to 26 days (**Fig. 5D**). A combination
407 of a tenfold increase in function evaluations with an equal multiplication of the number of complexes in
408 the SCEUA routine (ngs; see details in Duan et al., 1992) results in a further reduction of standard
409 deviations on $\delta^{18}\text{O}_c$ (0.23‰) and age result (12 days). These tests show that returns in terms of model
410 precision quickly diminish with increasing processing time. Since the total modelling time linearly
411 scales with the number of function evaluations, this tradeoff towards lower standard deviation on the
412 modelling result is costly. Since tThese function evaluations are repeated in each modelling window,
413 so the cost in terms of extra processing time can increase quickly, especially for larger $\delta^{18}\text{O}_c$ datasets.
414 In addition, in this situation the mean model offset (accuracy of the model; 7 days, 28 days and 14
415 days for maxn of $1.0 * 10^4$, $5.0 * 10^4$ and $1.0 * 10^5$ respectively; **Fig. 5D**) does not significantly improve
416 with increasing number of function evaluations. Based on these results, the default maxn parameter in
417 ShellChron was set to 10^4 to compromise between keeping modelling times short while retaining high
418 model accuracy. However, specific datasets may benefit from an increase in modeling time, so case-
419 by-case assessment of the optimal SCEUA parameters is recommended. A detailed evaluation of the
420 total modelling time in a typical $\delta^{18}\text{O}_c$ dataset is discussed in **section 4.4**.

421

422



423 **Figure 6:** Result of applying ShellChron on two virtual datasets: **Case 1** (top, see [SI8](#)) and **Texel**,
 424 (bottom, see [SI9](#)). Leftmost panels (**A** and **D**) show the model fit of individual sample windows (red) on
 425 the data (black, including horizontal and vertical error bars), with in the top left Spearman's correlation
 426 coefficients (ρ) and standard deviations on the $\delta^{18}\text{O}_c$ estimate (σ_{est}). Middle panels (**B** and **E**) show the
 427 resulting age model (red, including shaded 95% confidence level) compared with the [realknown](#) age-
 428 distance relationship of both records. Histograms in the top left of age-distance plots show the offset
 429 between modelled and measured $\delta^{18}\text{O}_c$ (as visualized in panels **A** and **D**) with standard deviations of
 430 the $\delta^{18}\text{O}_c$ offset (σ_{off}) and offset averages (μ). Histograms in the bottom right of age-distance plots show
 431 the offset between modelled and [actual-known](#) ages (in days) of each datapoint, including standard
 432 deviations on the age accuracy (σ_{acc}) and mean age offset (μ). Rightmost panels (**C** and **F**) highlight age
 433 offsets binned in [12](#) monthly time bins [based on their position relative to the annual cycle](#) to illustrate
 434 how accuracy varies over the seasons. Grey envelopes indicate 95% confidence levels on the monthly
 435 age offset [within these monthly time bins](#). [The horizontal red dashed line indicates no offset \(modelled](#)
 436 [age is equal to the known age of the sample\).](#)

437

438 **4.2 Artificial carbonate records**

439 Results of running ShellChron on [the Test case \(Fig. 4\)](#), **Case 1** and **Texel** datasets (Fig. 6) show that
440 modelled $\delta^{18}\text{O}_c$ records in individual windows closely match the data. [On the level of individual windows,](#)
441 [inter-annual growth rate variability is more difficult to model than the temperature sinusoid, especially](#)
442 [when sampling resolution is limited and at the beginning and end of the record \(Fig. 4B\)](#). However, after
443 [overlapping multiple windows, the accuracy of ShellChron improves significantly \(Fig. 4E\)](#). Note that in
444 [Fig. 4A-C, the length of the first model window \(difference in age between first and 11th datapoint\) is](#)
445 [less than 365 days, because the 12th datapoint, which occurs exactly 1 year after the first point, is not](#)
446 [part of the window](#). A summary of ShellChron performance statistics is given in **Table 2**. In all virtual
447 datasets, $\delta^{18}\text{O}_c$ estimates are equally distributed above and below the $\delta^{18}\text{O}_c$ data ($\Delta^{18}\text{O}_c = 0.0\text{‰}$;
448 Spearman's ρ of [0.94](#), [0.98](#) and [0.92](#) for [Test case](#), **Case 1** and **Texel** datasets respectively). Age
449 offsets vary slightly over the seasons, but the difference between monthly time bins is not statistically
450 significant on a 95% confidence level (Fig. 6C and F; see also SI12). The fact that seasonal bias in age
451 offset is absent in the **Texel** dataset, which is skewed towards growth in the winter season and includes
452 relatively strong seasonal variability in $\delta^{18}\text{O}_w$, shows that ShellChron is not sensitive to such subtle
453 (though common) variability in growth rate or $\delta^{18}\text{O}_w$. In general, ShellChron's mean age assignment is
454 accurate on a monthly scale (age offsets of $4 \pm 12\text{ d}$ and $+30 \pm 24\text{ d}$ for **Case 1** and **Texel** datasets
455 respectively). [However, age results in individual months do sometimes show significant offsets from the](#)
456 [known value \(e.g. Fig. 6C and 6F\)](#). This is most notable in **Case 1**, where accuracy of the age model
457 [decreases near the extreme values of the \$\delta^{18}\text{O}_c\$ curve \(Fig. 6B-C\)](#). This occurs because in these places
458 [the model is most sensitive to stochastic noise \(simulated uncertainty\) on the \$\delta^{18}\text{O}_c\$ value](#). A small
459 [random change in the \$\delta^{18}\text{O}_c\$ value at the minima or maxima of the \$\delta^{18}\text{O}_c\$ curve thus results in a large](#)
460 [change in the model fit of the \$\delta^{18}\text{O}_c\$ curve, resulting in a seasonally non-uniform decrease in the accuracy](#)
461 [of the model, as is evident from the skewed \$\Delta^{18}\text{O}_c\$ distribution in Figure 6B-C](#). The sampling resolution
462 in the **Texel** data decreases near the end of the record (see SI9), but this does not result in reduced age
463 model accuracy. If anything, the age of **Texel** samples is better approximated near the end of the record,
464 and age offsets are larger in the central part of the record ($\sim 30\text{-}50\text{ mm}$; Fig. 6E). The lower accuracy in
465 the third to fifth year of the **Texel** record is likely a result of the sub-annual variability in the record that
466 is superimposed on the seasonal cycle. [The lower sampling resolution later in the record mutes this](#)
467 [variability and illustrates that](#) [This variability is less pronounced near the end of the record, partly because](#)

Formatted: Superscript

Formatted: Superscript

Formatted: Not Superscript/ Subscript

468 this variability is not resolved at lower sampling resolution, which illustrates that higher sampling
469 resolutions do not necessarily result in better age models. The constant offset of the modelled age of
470 the Texel sample from the known age is a result of the way the model result was aligned to start at zero
471 for comparison with the known age (Fig. 6F). This was done by adding the offset from zero of the
472 modelled age of the first datapoint in the record to the entire record, thereby defining an arbitrary
473 reference point which is sensitive to the uncertainty on the age of the first sample (see also Oyster and
474 Speleothem results in Fig. 7B-C). Note that this alignment issue does not play a role in fossil data,
475 where model results can be aligned to growth marks in the carbonate (e.g. shell growth breaks or
476 laminae) and that it does not affect the seasonal alignment of proxy binned into monthly sample bins.

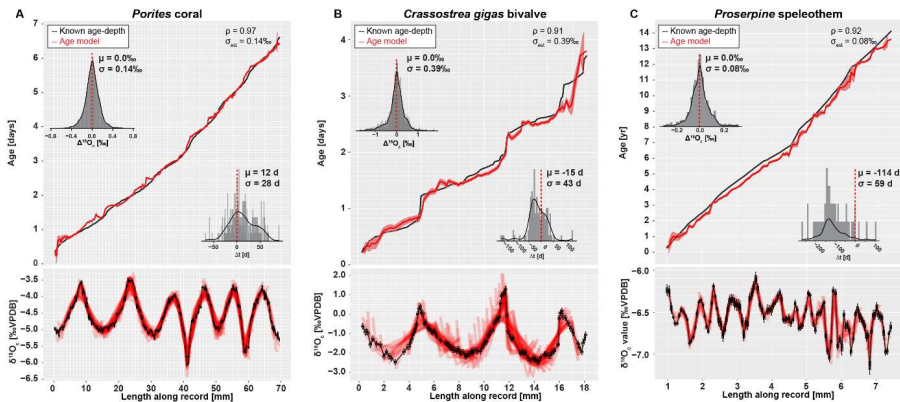
477

Formatted: Font: Not Bold

Table 2: Overview of datasets and model results

Dataset	Resolution	Length	$\delta^{18}\text{O}_c$ seasonal range	Complications
Test case	7–12 yr ⁻¹	5 yr	~5‰	Variable $\delta^{18}\text{O}_w$, Variable GR
Case 1	50 yr ⁻¹	6 yr	~4.3‰	None
Texel	26–45 yr ⁻¹	10 yr	~4‰	Variable $\delta^{18}\text{O}_w$, Variable GR
Coral	30–49 yr ⁻¹	6 yr	~1.7‰	Variable GR
Oyster	23–45 yr ⁻¹	3.5 yr	~3‰	Variable $\delta^{18}\text{O}_w$, Variable GR
Speleothem	4–13 yr ⁻¹	14 yr	~0.5‰	Variable $\delta^{18}\text{O}_w$, Variable GR, Non-sinusoidal $\delta^{18}\text{O}_c$ -forcing

Dataset	$\delta^{18}\text{O}_c$ offset ($\pm 1\sigma$)	Age offset ($\pm 1\sigma$)	Spearman's ρ	Observations
Test case	0.0 \pm 0.49 ‰	7 \pm 32 d	0.94	Slightly out of phase
Case 1	0.0 \pm 0.27‰	4 \pm 12 d	0.98	-
Texel	0.0 \pm 0.41‰	30 \pm 24 d	0.92	-
Coral	0.0 \pm 0.14‰	12 \pm 28 d	0.97	-
Oyster	0.0 \pm 0.39‰	-15 \pm 43 d	0.91	Reduced accuracy near growth stops
Speleothem	0.0 \pm 0.08‰	-114 \pm 59 d	0.92	Susceptible to phase offsets; Only reliable on inter-annual scale



479

480 **Figure 7:** Overview of model results for the three test datasets from real carbonate archives: **(A) coral**,
 481 **(B) oyster** and **(C) speleothem**. Lower panels indicate the fit of individual model windows (in red) with
 482 the data (in black) while upper panels show the age model (in red) compared to the “true” age-distance
 483 relationship with histograms showing model accuracy (in days, top left) and model fit ($\delta^{18}\text{O}_\text{c}$ offset in ‰,
 484 bottom right). Color scheme follows **Figure 3**. Note that the true age-distance relationship is not known
 485 for these natural records, but is estimated using known growth seasonality (**coral**), comparison with *in*
 486 *situ* temperature and salinity measurements (**oyster**) or simply by interpolating between annual growth
 487 lines (**speleothem**). See **Supplementary Methods** for details and **SI10** for raw data.

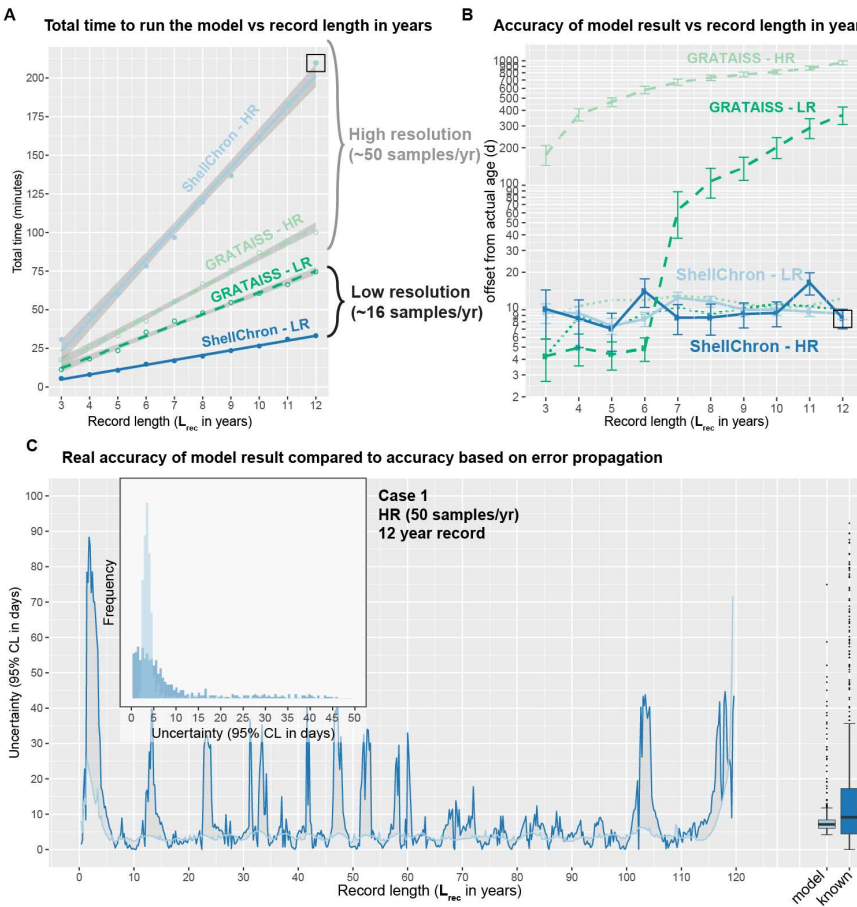
488

489 **4.3 Natural carbonate records**

490 Results of modelling natural carbonate records (**Fig. 7**; **Table 2**; see also **SI10**) illustrate the
491 effectiveness of ShellChron on different various types of records. Performance clearly depends on the
492 resolution of the record and the regularity of seasonal variability contained within. As in the virtual
493 datasets, modelled $\delta^{18}\text{O}_c$ successfully mimic $\delta^{18}\text{O}_c$ data in all records ($\Delta^{18}\text{O}_c = 0.0$; Spearman's ρ of
494 0.97, 0.91 and 0.92 for **coral**, **oyster** and **speleothem** respectively). No consistent seasonal bias is
495 observed in $\Delta^{18}\text{O}_c$ and model accuracy ($p > 0.05$; see **Table 2** and **SI12**), despite significant (seasonal
496 and inter-annual) variability contained in the records (especially in **oyster** and **speleothem** records).
497 When comparing the accuracy of these records, it must be noted that the "reknown" age of the samples
498 in these natural carbonates is not known. Model results are instead compared with age models
499 constructed using conventional techniques such as matching $\delta^{18}\text{O}_c$ profiles with local temperature
500 and/or $\delta^{18}\text{O}_w$ variability (**oyster** and **coral** records) or even merely by linear interpolation between annual
501 markers in the record (**speleothem** record; see **Supplementary Methods**). Despite this caveat, testing
502 results clearly show that the least complicated record (**coral**; **Fig. 7A**), characterized by minimal
503 variability in $\delta^{18}\text{O}_w$ and growth rate and a high sampling density, has the best overall model result ($\Delta^{18}\text{O}_c$
504 = 0.0 ± 0.14 compared to a $\sim 1.7\text{‰}$ seasonal range; $\rho = 0.97$; $\Delta t = 12 \pm 28$ d; see **Table 2**). The **oyster**
505 record (**Fig. 7B**), which has strong seasonal variability in growth rate and $\delta^{18}\text{O}_w$ also yields a very
506 reliable age model ($\Delta^{18}\text{O}_c = 0.0 \pm 0.39$ compared to a $\sim 3\text{‰}$ seasonal range; $\rho = 0.91$; $\Delta t = -15 \pm 43$ d;
507 see **Table 2**). On closer inspection, the age within the **oyster** record is clearly more difficult to model
508 than within the **coral**, due in part to the higher variability of $\delta^{18}\text{O}_c$ values superimposed on the seasonal
509 cycle, the sharp growth cessations in the winters (high $\delta^{18}\text{O}_c$ values) and the variability in sampling
510 resolution within the record. The latter causes the first growth year of the **oyster** record to be less
511 accurately modelled (**Fig. 7B**) while the variability in $\delta^{18}\text{O}_c$ causes the edges of some modelling windows
512 to predict steep increases or decreases in $\delta^{18}\text{O}_c$ (vertical "offshoots" in modelled $\delta^{18}\text{O}_c$; **Fig. 7B**). Note
513 that the low weighting of the edges of modelling windows combined with the high overall sampling
514 resolution in the **oyster** record minimizes the effect of these "offshoots" on the accuracy of the model.
515 The **speleothem** record (**Fig. 7C**), plagued by lower sampling resolution, large inter-annual $\delta^{18}\text{O}_c$
516 variability, restricted $\delta^{18}\text{O}_c$ seasonality and a lack of clearly seasonal $\delta^{18}\text{O}_c$ forcing, yields the least
517 reliable model result ($\Delta^{18}\text{O}_c = 0.0 \pm 0.08\text{‰}$ compared to a $\sim 0.5\text{‰}$ seasonal range; $\rho = 0.92$; $\Delta t = -114 \pm$
518 59 d; see **Table 2**). Note that the accuracy figure provided for the **speleothem** record is based on

519 comparison with an age model [based relying](#) on linear interpolation between annual growth lines. This
520 assumption of the age-distance relationship is almost certainly erroneous, since drip water supply to
521 (and therefore growth in) [speleothems](#) has been shown to vary seasonally (e.g. Baldini et al., 2008),
522 including at the very site the **speleothem** data derives from (Han-sur-Lesse cave, Belgium; Van
523 Rampelbergh et al., 2014; Vansteenberghe et al., 2019). However, since no reliable information is
524 available on sub-annual variability in growth rates in this record, ShellChron results cannot be validated
525 at the sub-annual scale in this case. The high age offset (-114 days) in the **speleothem** model result is
526 a consequence of the assumption in ShellChron that the highest temperature (lowest $\delta^{18}\text{O}_c$ value)
527 recorded in each growth year happens halfway through the year (day 183) [and the alignment of the](#)
528 [modelled age with the "known" age for this record \(see discussion of Texel results in 4.2\)](#). While [the](#)
529 assumption [about the phase of the temperature sinusoid](#) is approximately valid for temperature-
530 controlled $\delta^{18}\text{O}_c$ records (see **Fig. 6** and **7**), it is problematic for speleothems, in which $\delta^{18}\text{O}_c$ is often
531 dominated by the $\delta^{18}\text{O}_w$ of drip water, which may not be lowest during the summer season (see Van
532 Rampelbergh et al., 2014). The timing of the $\delta^{18}\text{O}_c$ minimum can be set in the *run_model* function using
533 the *t_maxtemp* parameter. Note that changing *t_maxtemp* does not affect relative dating within the $\delta^{18}\text{O}_c$
534 record, but, if set correctly, results in a phase shift of the age model result into better alignment with the
535 seasonal cycle.

536



537

538 **Figure 8:** Overview of the result of timing ShellChron and the [GRATAISS model](#) Judd et al. (2018) model
 539 on the same datasets (A), comparing the accuracies of both models (B) and comparing the accuracy
 540 as calculated by ShellChron with the [realknown](#) offset in the age model (C). In (A) and (B), low resolution
 541 datasets are plotted in dark blue ([ShellChron](#)) and dark green ([GRATAISS](#)), while high-resolution
 542 datasets plot in light blue ([ShellChron](#)) and light green ([GRATAISS](#)). Solid lines represent ShellChron
 543 and dashed lines show performance of the [GRATAISS model](#) Judd et al. model. Green dotted lines in
 544 (B) show the accuracies of the GRATAISS model on a year-by-year basis (without accumulating error
 545 due to linking consecutive years). The black box in (A) and (B) highlights the dataset used in (C). In (C),
 546 dark blue lines, bars and boxplot indicate true offset of the model from the actual sample age, while light

Formatted: Font: Not Bold

547 blue lines, bars and boxplot show the accuracy of the model as calculated from the propagated errors
548 on model and input data. Raw data is provided in **SI11**.

549 **4.4 Modeling time**

550 The performance of both ShellChron and [GRATAISS](#)~~the Judd et al. model~~ in terms of computation time
551 linearly increases with the length of the record (in years; see **Fig. 8**, **Fig. S5** and **SI11**). Computation
552 time of ShellChron on the high-resolution test dataset (50 samples/yr) increases very steeply with the
553 length of the record in years (~20 minutes per additional year), while the low-resolution dataset (16
554 samples/yr) shows a slower increase (~3 minutes per additional year; **Fig. 5A**). This contrasts with
555 [GRATAISS](#)~~the model from Judd et al.~~, which requires only slightly more time on high-resolution data
556 than on low-resolution datasets (~7 and ~10 minutes per additional year, respectively). The difference
557 is explained by the sliding window approach applied in ShellChron, which requires more SCEUA
558 optimization runs per year in high-resolution datasets than in low resolution datasets. When plotted
559 against the number of calculation windows or samples in the dataset, running ShellChron on low-
560 resolution and high-resolution datasets require a similar increase in computation time (~0.4 minutes, or
561 24 seconds, per additional sample/window; **Fig. S5**) under default SCEUA conditions. ShellChron ~~thus~~
562 outcompetes [GRATAISS](#)~~the Judd et al. model~~ in terms of computation time in datasets with fewer than
563 ~20 samples per year, even though more SCEUA optimizations are required.

564 [The A](#) key computational improvement in ShellChron is the application of a sinusoidal regression before
565 each SCEUA optimization to estimate the initial values of the modelled parameters (*sinreg* function; see
566 **equation 9** and **Fig. 1** in **Model description**). Since carbonate archives are rarely sampled for stable
567 isotope measurements above 20 samples per year (e.g. Goodwin et al., 2003; Schöne et al., 2005;
568 Lough, 2010 and references therein), the disadvantage of a steep computational increase for very high-
569 resolution archives is, in practice, a favorable tradeoff for the added control on model and measurement
570 uncertainty and smoother inter-year transitions ShellChron offers in comparison to previous models.
571 The similarity of ShellChron's accuracy in the low- and high-resolution datasets demonstrates its
572 robustness across datasets with various sampling resolutions (see also **Table 2** and **Fig. 7**).

573 Longer computation times in ~~the Judd et al. model~~[GRATAISS](#) result in slightly better accuracy on the
574 modelled age compared to ShellChron on the scale of individual datapoints in low-resolution datasets
575 (see **Fig. 8B**). However, this advantage is rapidly lost when records containing multiple years are
576 considered (**Fig. 8B**). The advantage of the ShellChron model is its application of overlapping model
577 windows, which smooth out the transitions between modelled years and eliminate accumulations of

578 model inaccuracies when records grow longer. In addition, contrary to previous models, ShellChron
579 does not rely on user-defined year boundaries, which may introduce mismatches between subsequent
580 years to be propagated through the age model, even in ideal datasets such as **Case 1** (Fig. 8B; see
581 also **Supplementary Methods**). By comparison, the overall accuracy of ShellChron is much more stable
582 within and between datasets of different length, while rarely introducing offsets of more than a month. It
583 must be noted here that the cumulative, multi-year age uncertainty in the GRATAISS model (Fig. 8B)
584 was calculated by combining the results of consecutive growth years in the record, which the GRATAISS
585 model models separately, while avoiding age inversions and retaining the seasonal phase of the model
586 results. This procedure causes gaps in time to be introduced in the cumulative age modelled by
587 GRATAISS whenever the results of two consecutive, individually modelled growth years do not align,
588 explaining the sharp increases in age uncertainty of the GRATAISS model result (Fig. 8B). These
589 cumulative uncertainties are therefore not theoretically part of the model result (see year-by-year
590 uncertainty in Fig. 8B) but are a necessary consequence of the way GRATAISS approximates growth
591 years separately. If only within-year inaccuracies are compared, GRATAISS results are roughly equally
592 accurate as ShellChron results (see dotted lines in Fig. 8B).

593 More importantly, w\Where ShellChron takes into account considers the uncertainty on input parameters,
594 this uncertainty is not considered in most previous models (the MoGroFun model of Goodwin et al.,
595 2003 being the exception). The added uncertainty caused by input error is higher in less regular
596 (sinusoidal) $\delta^{18}\text{O}_\text{c}$ records and in records with lower sampling resolution, causing the uncertainties on
597 the Judd et al., modelGRATAISS reported here for the ideal, high-resolution **Case 1** dataset to be over-
598 optimistic. If ShellChron's model accuracy is insufficient, its modular character allows the user to run the
599 SCEUA algorithm to within more precise optimization criteria by changing the model parameters (see
600 **section 4.1**). However, this adaptation comes at a cost of longer computation times.

601 The estimated uncertainty envelope (95% confidence interval) on the modelled age calculated by the
602 error propagation algorithm in ShellChron (4.7 ± 6.5 d) on average slightly underestimates the actual
603 offset between modelled age and realknown age in the **Case 1** record (9.3 ± 13.1 d; Fig. 8C). The
604 foremost difference between modelled and realknown uncertainty on the result is that the modelled
605 uncertainty yields a more smoothed record of uncertainty compared to the record of actual offset of the
606 model (Fig. 8C). ShellChron's uncertainty calculations are partly based on comparing overlapping
607 model windows, thereby smoothing out short term variations in model offset. The uncertainty of the

608 model result (both realknown and modelled) shows regular variability with a period of half a year (**Fig.**
609 **8C**). Comparing this variability with the phase of the record (of which 6 years are plotted in **Fig. 6A**)
610 reveals that the uncertainty of the model is positively-negatively correlated to the slope of the $\delta^{18}\text{O}_c$
611 record. This is expected, because in parts of the record with steep- $\delta^{18}\text{O}_c$ -distance-slopesextreme
612 values in the $\delta^{18}\text{O}_c$ curve, the local age model result is more sensitive to small changes in the
613 sampling distance, caused either by uncertainty in the model fit or propagated uncertainty on the
614 sampling distance defined by the user (see discussion in section 4.2). The slight seasonal variability in
615 model accuracy in **Case 1** is also shown in **Fig. 6C** and comprises a difference in uncertainty of up to
616 10 days depending on the time of year in which the datapoint is found.

Formatted: Font: (Default) Arial

Formatted: Font: (Default) Arial, 10 pt

617 **5. Applications and discussion**

618 Its new features compared to previous age model routines make ShellChron a versatile package for
619 creating age models in a range of high-resolution paleoclimate records. The discussion above
620 demonstrates that ShellChron can reconstruct the age of individual $\delta^{18}\text{O}_c$ samples within monthly
621 precision. This level of precision is sufficient for accurate reconstructions of seasonality, defined as the
622 difference between warmest and coldest month (following USGS definitions; O'Donnell and Ignizio,
623 2012). While an improvement on this uncertainty could be of potential interest for ultra-high-resolution
624 paleoclimate studies (e.g. sub-daily variability, see Sano et al., 2012; Yan et al., 2020; de Winter et al.,
625 2020a), the increase in computation time and the sampling resolution such detailed age models demand
626 render age modelling from $\delta^{18}\text{O}_c$ records inefficient for this purpose (see **sections 4.1 and 4.4**). The
627 sampling resolution for high-resolution carbonate $\delta^{18}\text{O}_c$ records in the literature does not typically exceed
628 100 μm due to limitations in sampling acquisition (e.g. micromilling), which even in fast-growing archives
629 limits the resolution of these records to several days at best (see Gagan et al., 1994; Van Rampelbergh
630 et al., 2014; de Winter et al., 2020c). While in some archives, high-resolution ($< 100 \mu\text{m}$) trace element
631 records could be used to capture variability beyond this limit, the monthly age resolution of ShellChron
632 is sufficient for most typical high-resolution paleoclimate studies.

633 The ability to produce uninterrupted age models from multi-year records while considering both
634 variability in $\delta^{18}\text{O}_w$ and uncertainties on input parameters represent major advantages of ShellChron
635 over previous age modelling solutions. As a result, ShellChron can be applied on a wide range of
636 carbonate archives (see **Fig. 7** and **Table 2**). However, testing ShellChron on different records highlights
637 the limitations of the model inherited through its underlying assumptions. The most accurate model
638 results are obtained on records with minimal growth rate and $\delta^{18}\text{O}_w$ variability and a nearly sinusoidal
639 $\delta^{18}\text{O}_c$ record, such as tropical **coral** records (**Fig. 7A**; Gagan et al., 1994). In records where large
640 seasonal variability in growth rate and $\delta^{18}\text{O}_w$ does occur, such as in intertidal **oyster** shells, ShellChron's
641 accuracy slightly decreases, especially near growth hiatuses in the record (see **Fig. 7B**; Ullmann et al.,
642 2010). A worst-case scenario is represented by the **speleothem** record, which not only suffers from
643 much slower and more unpredictable growth rates and contains a comparatively small annual range in
644 $\delta^{18}\text{O}_c$, but it responds to $\delta^{18}\text{O}_w$ variability in drip water in the cave rather than temperature seasonality,
645 one of the assumptions underlying the current version of ShellChron (**Fig. 7C**; Vansteenberghe et al.,

646 2019). Despite these problems, ShellChron yields an age model that is remarkably accurate on an
647 annual timescale, which is as good as, or better than, the best age model that can be obtained by
648 applying layer counting on the most clearly laminated parts of the speleothem (e.g. Verheyden et al.,
649 2006). It must be noted that, while the close fit between modelled $\delta^{18}\text{O}_c$ and **speleothem** $\delta^{18}\text{O}_c$ data (ρ
650 = 0.92; $\sigma = 0.08\text{‰}$) is encouraging, a major reason for the model's success is the fact that the Proserpine
651 speleothem used in this example is known to receive significantly seasonal (though not sinusoidal) drip
652 water volumes and concentrations (Van Rampelbergh et al., 2014). Variability in drip water properties
653 and cave temperatures are known to differ strongly between cave systems (Fairchild et al., 2006;
654 Lachniet, 2009). For ShellChron (or any other $\delta^{18}\text{O}_c$ -based age model) to work reliably in speleothem
655 records, consistent seasonal variability in either temperature or $\delta^{18}\text{O}_w$ should be demonstrated to
656 significantly influence the $\delta^{18}\text{O}_c$ variability in the record. In practice, these constraints make ShellChron
657 applicable in speleothems for which the cave environment varies in response to the seasonal cycle,
658 such as localities overlain by thin epikarst, well-ventilated caves or speleothems situated close to the
659 cave entrance (Verheyden et al., 2006; Feng et al., 2013; Baker et al., 2021).

660 ShellChron's ability to model multi-year records with smooth transitions between the years does not
661 compromise the accuracy of its age determination on the seasonal scale (e.g. Fig. 6 and 7). Many
662 paleoclimatology studies investigating the seasonal cycle rely on stacking of seasonal variability relative
663 to the annual cycle, thereby combining seasonal information from multiple years to obtain a precise
664 reconstruction of seasonal variability in the past (e.g. de Winter et al., 2018; Judd et al., 2019; Tierney
665 et al., 2020). While this can be achieved using age models of individual years (e.g. Judd et al., 2018),
666 seasonally resolved archives dated using ShellChron can also be stacked along a common seasonal
667 axis while retaining information about the multi-annual record allowing, for example, comparison
668 between consecutive years dated using the same age model including uncertainty on the age
669 determination.

Formatted: Font: Not Bold

670 The difficulty of applying age model routines on speleothem records highlights one of the main
671 advantages of ShellChron over pre-existing age model routines, namely its modular character. Since
672 $\delta^{18}\text{O}_c$ records from some carbonate archives, such as speleothems, cannot be described by the
673 standard combination of temperature and growth rate sinusoids on which ShellChron is based (in its
674 current version), the possibility to adapt the "building block" functions used to approximate these $\delta^{18}\text{O}_c$

675 records (*d18O_model*, *temperature_curve* and *growth_rate_curve*; see **Fig. 1**) while leaving the core
676 structure of ShellChron intact greatly augments the versatility of the model. The freedom to adapt the
677 building blocks used to approximate the $\delta^{18}\text{O}_c$ record theoretically enables ShellChron to model sub-
678 annual age-distance relationships in any record **as long as** the seasonal variability in the variables used
679 to model the input data are predictable and can be represented by a function. For example, since
680 speleothem $\delta^{18}\text{O}_c$ records often depend on variability in the $\delta^{18}\text{O}_w$ value of the drip water, a function
681 describing this variability through the year can replace the *temperature_curve* function to create more
682 accurate sub-annual age models for speleothems (e.g. Matthey et al., 2008; Lachniet, 2009; Van
683 Rampelbergh et al., 2014). Similarly, the *growth_rate_curve* function can be modified in case the default
684 skewed sinusoid does not accurately describe the extension rate of the record under study, and the
685 *d18O_model* function can be adapted to feature the most fitting $\delta^{18}\text{O}_c$ -temperature or $\delta^{18}\text{O}_c$ - $\delta^{18}\text{O}_w$
686 relationship. Note that the flexibility of this approach is limited by the expression of the annual cycle in
687 the $\delta^{18}\text{O}_c$ record. The $\delta^{18}\text{O}_c$ -based dating approach in ShellChron will therefore have **severe more**
688 trouble dating records in which the annual $\delta^{18}\text{O}_c$ variability is severely damped, such as speleothems
689 in deeper cave systems (e.g. Vansteenberghe et al., 2016), or in which annual $\delta^{18}\text{O}_c$ variability is not
690 sinusoidal, such as tropical records with bimodal temperature or precipitation seasonality (Knoben et
691 al., 2018).

692 Flexibility in the definition of “building block” functions used to approximate the input data paves the way
693 for future application beyond carbonate $\delta^{18}\text{O}_c$ records. The seasonal variability in $\delta^{18}\text{O}$ in some ice cores
694 can be approximated by a stable and unbiased temperature relationship (van Ommen and Morgan,
695 1997). ShellChron can therefore be modified to date sub-annual samples in these ice core records and
696 reconstruct seasonal variability in the high latitudes through the **QuaternaryQuaternary**. Similarly, inter-
697 annual $\delta^{18}\text{O}$ variability in tree ring records are demonstrated to record variability in precipitation through
698 the year, and this variability can be modelled to improve sub-annual age models in these records (Xu et
699 al., 2016). More generally, the field of dendrochemistry has recently developed additional chemical
700 proxies for seasonality (e.g. trace element concentrations), which can be measured on smaller sample
701 volumes (and thus greater resolution) to obtain ultra-high-resolution records on which (sub-annual)
702 dating can be based (e.g. Poussart et al., 2006; Superville et al., 2017). A similar development has taken
703 place in the study of carbonate bio-archives such as corals and mollusks, of which some show strong,
704 predictable seasonal variability in trace elements (e.g. Mg/Ca and Sr/Ca ratios) which can be used to

705 accurately date these records (de Villiers et al., 1995; Sosdian et al., 2006; Durham et al., 2017; [de](#)
706 [Winter et al., 2021b](#)). Minor changes in the “building block” functions using empirical transfer functions
707 for these trace element records will enable ShellChron to capitalize on these relationships and
708 reconstruct sub-annual growth rates with improved precision due to the higher precision with which
709 these proxies can be measured compared to $\delta^{18}\text{O}_c$ records. Finally, the application of ShellChron for
710 age model construction is not necessarily limited to the seasonal cycle, as other major cycles in climate
711 (e.g. tidal, diurnal or Milankovitch cycles) leave similar marks on climate records and can thus be used
712 as basis for age modelling (e.g. Sano et al., 2012; Huyghe et al., 2019; de Winter et al., 2020a; Sinnesael
713 et al., 2020). It must be noted that, since ShellChron was developed for modeling based on annual
714 periodicity, applying it on other timescales would require more thorough adaptation of the model code
715 than merely adapting the “building block” functions to support additional proxy systems.

716 While age reconstructions are the main aim of ShellChron, the model also yields information about the
717 temperature and growth rate parameters used in each simulation window to approximate the local $\delta^{18}\text{O}_c$
718 curve (see *parameter matrix* in **Fig. 1** and **SI6**). These parameters hold key information about the
719 response of the archive to seasonal changes in the environment, such as the season of growth,
720 relationships between growth rate and temperature and the temperature range that is recorded.
721 Combining these parameters with records of influential environmental variables such as seawater
722 chlorophyll concentration or local precipitation patterns yields information about the response of the
723 climate archive to environmental variables, in addition to the climate or environmental change it records.
724 Study examples include the relationship between growth rate of marine calcifies and phytoplankton
725 abundance or the correlation between precipitation patterns and chemical variability in speleothems.
726 While such discussion is beyond the scope of this work, examples of parameter distributions are
727 provided in **SI5**, and the application of modelled growth rate parameters in bivalve sclerochronology is
728 discussed in more detail in Judd et al. (2018). Note that the sliding window approach of ShellChron
729 produces records of changing temperature and growth rate parameters at the scale of individual
730 samples (albeit smoothed by the sliding window approach) rather than annually, as in Judd et al. (2018).

731

732 **6. Conclusions**

733 ShellChron offers a novel, open-source solution to the problem of dating carbonate archives for high-
734 resolution paleoclimate reconstruction on a sub-annual scale. Based on critical evaluation of previous
735 age models, building on their strengths while attempting to eliminate–minimize their weaknesses,
736 ShellChron provides continuous age models based on $\delta^{18}\text{O}_{\text{c}}$ -profiles in these archives with monthly
737 accuracy, considering the uncertainties associated with both the model itself and the input data. The
738 monthly accuracy of the model, as tested on a range of virtual and natural datasets, enables its
739 application for age determination in studies of seasonal climate and environmental variability. Higher
740 accuracies can be reached at the cost of longer computation times by adapting the model parameters,
741 but age determinations far beyond the monthly scale are unlikely to be feasible considering the
742 limitations on sampling resolution and measurement uncertainties on $\delta^{18}\text{O}_{\text{c}}$ records. ShellChron's
743 computation times on datasets with sampling resolutions typical for the paleoclimatology field (up to 20
744 samples/yr) remain practical and comparable to previous model solutions, despite adding several
745 features that improve the versatility and interpretation of model results. Its modular design allows
746 ShellChron to be adapted to different situations with comparative ease. It thereby functions as a platform
747 for age-distance modelling on a wide range of climate and environmental archives and is not limited in
748 its application to the $\delta^{18}\text{O}_{\text{c}}$ proxy, the carbonate substrate or even to the annual cycle, as long as the
749 relationship between the proxy and the extension rate of the archive on a given time scale can be
750 parameterized. Future improvements will capitalize on this variability, expanding ShellChron beyond its
751 current dependency on the $\delta^{18}\text{O}_{\text{c}}$ -temperature relationship in carbonates. Members of the high-
752 resolution paleoclimate community are invited to contribute to this effort by adapting the model for their
753 purpose.

754

755 **Code availability**

756 ShellChron is worked out into a fully functioning package for the open-source computational language
757 R (version 3.5.0 or later; R Core Team, 2020). The most recent full version (v0.4.0) of the ShellChron
758 passed the code review of the Comprehensive R Archive Network (CRAN) and is freely available for
759 download as an R package on the CRAN server (see <https://CRAN.R-project.org/package=ShellChron>).
760 The CRAN server entry also includes detailed line-by-line documentation of the code and working
761 examples for every function. In addition, the latest development version of ShellChron is available on

762 GitHub (<https://github.com/niejsjewinter/ShellChron>). Those interested in adapting ShellChron for their
763 research purposes are invited to do so ~~there~~. Code and documentation, together with all supplementary
764 files belonging to this study, are also available on the open-source online repository Zenodo
765 (<http://doi.org/10.5281/zenodo.4288344>).

766

767 **Author contribution**

768 NJW designed the study, wrote the model script, carried out the test calculations and wrote the
769 manuscript.

770

771 **Competing interests**

772 There were no competing interests to declare.

773

774 **Acknowledgements**

775 This research project is part of the UNBIAS project funded by the European Commission through a
776 Marie Curie Individual Fellowship (MSCA-IF; grant number: 843011) and the Flemish Research Council
777 (FWO; junior postdoc grant, project number: 12ZB220N). Thanks go to Emily Judd for discussions about
778 the workings of the Judd et al. (2018) model and its potential adaptation beyond aragonitic mollusk
779 shells. High-resolution temperature and salinity data from the NIOZ jetty which underlie the **Texel**
780 dataset and the noise added to the idealized **Case 1** dataset were kindly provided by Eric Wagemaakers
781 and Sonja van Leeuwen (Royal Dutch Institute for Sea Research, the Netherlands). The $\delta^{18}\text{O}_c$ data
782 series from the *Crassostrea gigas* (**oyster**) and Proserpine stalagmite (**speleothem**) were generously
783 provided by dr. Clemens V. Ullmann (University of Exeter, UK) and dr. Stef Vansteenberge (Vrije
784 Universiteit Brussel, Belgium), respectively. Raw data from the *Porites lutea* **coral** dataset were obtained
785 with help of the WebPlotDigitizer (<https://automeris.io/WebPlotDigitizer/>) developed by Ankit Rohatgi.
786 Preparation of the ShellChron model into an R package would not have been possible without the helpful
787 instructions by Fong Chun Chan (<https://tinyheero.github.io/jekyll/update/2015/07/26/making-your-first-R-package.html>), Hilary Parker (<https://hilaryparker.com/2014/04/29/writing-an-r-package-from->

789 [scratch/](#)) and Hadley Wickham (<https://r-pkgs.org/release.html>) as well as the insightful and inspiring
790 discussions on R coding and statistics with Ilja Kocken (Utrecht University). In addition, distribution of
791 the code in an organized way was made possible thanks to Git (<https://git-scm.com/>) and Github
792 (<https://github.com/>) and the R Project Team (<https://www.r-project.org/>), with special thanks to Uwe
793 Ligges (University of Dortmund, Germany) and Gregor Seyer (University of Vienna, Austria) for their
794 comments on initial submissions of the package to the CRAN database. Thanks go to William A. Huber
795 (<https://www.analysisandinference.com/team/william-a-huber-phd>) for providing a practical general
796 solution to the peak identification problem in the *cumulative_day* function (see *peakid* function and
797 https://rpubs.com/mengxu/peak_detection).

798

799 **References**

800 Bajnai D., Guo W., Spötl C., Coplen T. B., Methner K., Löffler N., Krsnik E., Gischler E., Hansen M.,
801 Henkel D., Price G. D., Raddatz J., Scholz D. and Fiebig J. (2020) Dual clumped isotope thermometry
802 resolves kinetic biases in carbonate formation temperatures. *Nature Communications* **11**, 4005.

803 Baker A., Mariethoz G., Comas-Bru L., Hartmann A., Frisia S., Borsato A., Treble P. C. and Asrat A.
804 (2021) The Properties of Annually Laminated Stalagmites-A Global Synthesis. *Reviews of Geophysics*
805 **59**, e2020RG000722.

806 Baldini J. U. L., McDermott F., Hoffmann D. L., Richards D. A. and Clipson N. (2008) Very high-
807 frequency and seasonal cave atmosphere PCO₂ variability: Implications for stalagmite growth and
808 oxygen isotope-based paleoclimate records. *Earth and Planetary Science Letters* **272**, 118–129.

809 Brand W. A., Coplen T. B., Vogl J., Rosner M. and Prohaska T. (2014) Assessment of international
810 reference materials for isotope-ratio analysis (IUPAC Technical Report). *Pure and Applied Chemistry*
811 **86**, 425–467.

812 de Brauwere A., De Ridder F., Pintelon R., Schoukens J. and Dehairs F. (2009) A comparative study
813 of methods to reconstruct a periodic time series from an environmental proxy record. *Earth-Science
814 Reviews* **95**, 97–118.

815 Butler P. G., Wanamaker A. D., Scourse J. D., Richardson C. A. and Reynolds D. J. (2013) Variability
816 of marine climate on the North Icelandic Shelf in a 1357-year proxy archive based on growth
817 increments in the bivalve *Arctica islandica*. *Palaeogeography, Palaeoclimatology, Palaeoecology* **373**,
818 141–151.

819 Chauvaud L., Lorrain A., Dunbar R. B., Paulet Y.-M., Thouzeau G., Jean F., Guarini J.-M. and
820 Mucciarone D. (2005) Shell of the Great Scallop *Pecten maximus* as a high-frequency archive of
821 paleoenvironmental changes. *Geochemistry, Geophysics, Geosystems* **6**.

822 Coplen T. B. (2007) Calibration of the calcite–water oxygen-isotope geothermometer at Devils Hole,
823 Nevada, a natural laboratory. *Geochimica et Cosmochimica Acta* **71**, 3948–3957.

824 Daëron M., Drysdale R. N., Peral M., Huyghe D., Blamart D., Coplen T. B., Lartaud F. and Zanchetta
825 G. (2019) Most Earth-surface calcites precipitate out of isotopic equilibrium. *Nature Communications*
826 **10**, 429.

827 Daëron M., Guo W., Eiler J., Genty D., Blamart D., Boch R., Drysdale R., Maire R., Wainer K. and
828 Zanchetta G. (2011) ¹³C¹⁸O clumping in speleothems: Observations from natural caves and
829 precipitation experiments. *Geochimica et Cosmochimica Acta* **75**, 3303–3317.

830 De Ridder F., de Brauwere A., Pintelon R., Schoukens J., Dehairs F., Baeyens W. and Wilkinson B. H.
831 (2007) Comment on: Paleoclimatic inference from stable isotope profiles of accretionary biogenic
832 hardparts—a quantitative approach to the evaluation of incomplete data, by Wilkinson, BH, Ivany, LC,
833 2002. *Palaeogeogr. Palaeoecol. Palaeoecol.* 185, 95–114. *Palaeogeography, Palaeoclimatology,
834 Palaeoecology* **248**, 473–476.

835 DeCarlo T. M. and Cohen A. L. (2017) Dissements, density bands and signatures of thermal stress
836 in Porites skeletons. *Coral Reefs* **36**, 749–761.

837 Dettman D. L., Reische A. K. and Lohmann K. C. (1999) Controls on the stable isotope composition of
838 seasonal growth bands in aragonitic fresh-water bivalves (Unionidae). *Geochimica et Cosmochimica
839 Acta* **63**, 1049–1057.

840 Duan Q., Sorooshian S. and Gupta V. (1992) Effective and efficient global optimization for conceptual
841 rainfall-runoff models. *Water resources research* **28**, 1015–1031.

842 Dunbar R. B. and Wellington G. M. (1981) Stable isotopes in a branching coral monitor seasonal
843 temperature variation. *Nature* **293**, 453–455.

844 Durham S. R., Gillikin D. P., Goodwin D. H. and Dietl G. P. (2017) Rapid determination of oyster
845 lifespans and growth rates using LA-ICP-MS line scans of shell Mg/Ca ratios. *Palaeogeography,
846 Palaeoclimatology, Palaeoecology*.

847 Epstein S., Buchsbaum R., Lowenstam H. A. and Urey H. C. (1953) Revised carbonate-water isotopic
848 temperature scale. *Geological Society of America Bulletin* **64**, 1315–1326.

849 Evans M. N. and Schrag D. P. (2004) A stable isotope-based approach to tropical dendroclimatology
850 1Associate editor: D. W. Lea. *Geochimica et Cosmochimica Acta* **68**, 3295–3305.

851 Fairchild I. J., Smith C. L., Baker A., Fuller L., Spötl C., Matthey D., McDermott F., and others (2006)
852 Modification and preservation of environmental signals in speleothems. *Earth-Science Reviews* **75**,
853 105–153.

854 Feng W., Casteel R. C., Banner J. L. and Heinze-Fry A. (2014) Oxygen isotope variations in rainfall,
855 drip-water and speleothem calcite from a well-ventilated cave in Texas, USA: Assessing a new
856 speleothem temperature proxy. *Geochimica et Cosmochimica Acta* **127**, 233–250.

857 Frisia S., Borsato A., Fairchild I. J. and McDermott F. (2000) Calcite fabrics, growth mechanisms, and
858 environments of formation in speleothems from the Italian Alps and southwestern Ireland. *Journal of
859 Sedimentary Research* **70**, 1183–1196.

860 Gagan M. K., Chivas A. R. and Isdale P. J. (1994) High-resolution isotopic records from corals using
861 ocean temperature and mass-spawning chronometers. *Earth and Planetary Science Letters* **121**, 549–
862 558.

863 Goodwin D. H., Paul P. and Wissink C. L. (2009) MoGroFunGen: A numerical model for reconstructing
864 intra-annual growth rates of bivalve molluscs. *Palaeogeography, Palaeoclimatology, Palaeoecology*
865 **276**, 47–55.

866 Goodwin D. H., Schöne B. R. and Dettman D. L. (2003) Resolution and Fidelity of Oxygen Isotopes as
867 Paleotemperature Proxies in Bivalve Mollusk Shells: Models and Observations. *PALAIOS* **18**, 110–
868 125.

869 Grossman E. L. and Ku T.-L. (1986) Oxygen and carbon isotope fractionation in biogenic aragonite:
870 temperature effects. *Chemical Geology: Isotope Geoscience section* **59**, 59–74.

871 Huybers P. and Curry W. (2006) Links between annual, Milankovitch and continuum temperature
872 variability. *Nature* **441**, 329.

873 Huyghe D., de Rafelis M., Ropert M., Mouchi V., Emmanuel L., Renard M. and Lartaud F. (2019) New
874 insights into oyster high-resolution hinge growth patterns. *Mar Biol* **166**, 48.

875 IPCC, Masson-Delmotte, V., Zhai, P., Pirani, A., Connors, S. L., Péan, C., Berger, S., Caud, N., Chen, Y., Goldfarb, L., Gomis, M. I., Huang, M., Leitzell, K., Lonnoy, E., Matthews, J. B. R., Maycock, T. K., Waterfield, T., Yelekçi, Ö., Yu, R., and Zhou, B. (Eds.): Climate Change 2021: The Physical Science Basis. Contribution of Working Group I to the Sixth Assessment Report of the Intergovernmental Panel on Climate Change, Cambridge University Press, 2021. IPCC (2018) GLOBAL WARMING OF 1.5 °C an IPCC special report on the impacts of global warming of 1.5 °C above pre-industrial levels and related global greenhouse gas emission pathways, in the context of strengthening the global response to the threat of climate change, sustainable development, and efforts to eradicate poverty.,

883 Ivany L. C. and Runnegar B. (2010) Early Permian seasonality from bivalve $\delta^{18}\text{O}$ and implications for
884 the oxygen isotopic composition of seawater. *Geology* **38**, 1027–1030.

885 Ivany, L. C. and Judd, E. J.: Deciphering Temperature Seasonality in Earth's Ancient Oceans, 50,
886 123–152, <https://doi.org/10.1146/annurev-earth-032320-095156>, 2022.

887 Jones D. S. (1983) Sclerochronology: Reading the Record of the Molluscan Shell: Annual growth
888 increments in the shells of bivalve molluscs record marine climatic changes and reveal surprising
889 longevity. *American Scientist* **71**, 384–391.

890 Jones D. S. and Quiltyer I. R. (1996) Marking Time with Bivalve Shells: Oxygen Isotopes and Season
891 of Annual Increment Formation. *PALAIOS* **11**, 340–346.

892 Judd E. J., Wilkinson B. H. and Ivany L. C. (2018) The life and time of clams: Derivation of intra-annual
893 growth rates from high-resolution oxygen isotope profiles. *Palaeogeography, Palaeoclimatology,*
894 *Palaeoecology* **490**, 70–83.

895 Judd, E. J., Ivany, L. C., DeConto, R. M., Halberstadt, A. R. W., Miklus, N. M., Junium, C. K., and
896 Uveges, B. T.: Seasonally resolved proxy data from the Antarctic Peninsula support a heterogeneous
897 middle Eocene Southern Ocean. **34**, 787–799, 2019.

898 Kim S.-T. and O'Neil J. R. (1997) Equilibrium and nonequilibrium oxygen isotope effects in synthetic
899 carbonates. *Geochimica et Cosmochimica Acta* **61**, 3461–3475.

900 Knoben W. J. M., Woods R. A. and Freer J. E. (2019) Global bimodal precipitation seasonality: A
901 systematic overview. *International Journal of Climatology* **39**, 558–567.

902 Lachniet M. S. (2009) Climatic and environmental controls on speleothem oxygen-isotope values.
903 *Quaternary Science Reviews* **28**, 412–432.

904 Le Tissier M. D. A., Clayton B., Brown B. E. and Davis P. S. (1994) Skeletal correlates of coral density
905 banding and an evaluation of radiography as used in sclerochronology. *Marine Ecology Progress Series*
906 **110**, 29–44.

907 LeGrande A. N. and Schmidt G. A. (2006) Global gridded data set of the oxygen isotopic composition
908 in seawater. *Geophysical research letters* **33**.

909 Lough J. M. (2010) Climate records from corals. *WIREs Climate Change* **1**, 318–331.

910 Mahé K., Bellamy E., Lartaud F. and Rafélis M. de (2010) Calcein and manganese experiments for
911 marking the shell of the common cockle (*Cerastoderma edule*): tidal rhythm validation of increments
912 formation. *Aquat. Living Resour.* **23**, 239–245.

913 Matthey D., Lowry D., Duffet J., Fisher R., Hodge E. and Frisia S. (2008) A 53 year seasonally resolved
914 oxygen and carbon isotope record from a modern Gibraltar speleothem: Reconstructed drip water and
915 relationship to local precipitation. *Earth and Planetary Science Letters* **269**, 80–95.

916 McCrea J. M. (1950) On the Isotopic Chemistry of Carbonates and a Paleotemperature Scale. *J.
917 Chem. Phys.* **18**, 849–857.

918 Mitchell Jr. J. M. (1976) An overview of climatic variability and its causal mechanisms. *Quaternary
919 Research* **6**, 481–493.

920 Mohr R. C., Tobin T. S., Petersen S. V., Dutton A. and Oliphant E. (2020) Subannual stable isotope
921 records reveal climate warming and seasonal anoxia associated with two extinction intervals across
922 the Cretaceous–Paleogene boundary on Seymour Island, Antarctica. *Geology* **48**, 1131–1136.

923 Müller P., Taylor M. H., Klicpera A., Wu H. C., Michel J. and Westphal H. (2015) Food for thought:
924 Mathematical approaches for the conversion of high-resolution sclerochronological oxygen isotope
925 records into sub-annually resolved time series. *Palaeogeography, Palaeoclimatology, Palaeoecology*
926 **440**, 763–776.

927 O'Donnell M. S. and Ignizio D. A. (2012) Bioclimatic predictors for supporting ecological applications in
928 the conterminous United States. *US Geological Survey Data Series* **691**.

929 Ommen T. D. van and Morgan V. (1997) Calibrating the ice core paleothermometer using seasonality.
930 *Journal of Geophysical Research: Atmospheres* **102**, 9351–9357.

931 Poussart P. M., Myneni S. C. B. and Lanzirotti A. (2006) Tropical dendrochemistry: A novel approach
932 to estimate age and growth from ringless trees. *Geophysical Research Letters* **33**.

933 R Core Team (2020) *R: A Language and Environment for Statistical Computing*., R Foundation for
934 Statistical Computing, Vienna, Austria.

935 Rohling E. J. (2013) Oxygen isotope composition of seawater. *The Encyclopedia of Quaternary
936 Science*. Amsterdam: Elsevier **2**, 915–922.

937 Saenger C., Gabitov R. I., Farmer J., Watkins J. M. and Stone R. (2017) Linear correlations in bamboo
938 coral $\delta^{13}\text{C}$ and $\delta^{18}\text{O}$ sampled by SIMS and micromill: Evaluating paleoceanographic potential and
939 biomineralization mechanisms using $\delta^{11}\text{B}$ and Δ^{47} composition. *Chemical Geology* **454**, 1–14.

940 Sano Y., Kobayashi S., Shirai K., Takahata N., Matsumoto K., Watanabe T., Sowa K. and Iwai K.
941 (2012) Past daily light cycle recorded in the strontium/calcium ratios of giant clam shells. *Nature*
942 *Communications* **3**, 761.

943 Schöne B. R., Fiebig J., Pfeiffer M., Gleß R., Hickson J., Johnson A. L., Dreyer W. and Oschmann W.
944 (2005) Climate records from a bivalved Methuselah (*Arctica islandica*, Mollusca; Iceland).
945 *Palaeogeography, Palaeoclimatology, Palaeoecology* **228**, 130–148.

946 Schöne B. R. and Gillikin D. P. (2013) Unraveling environmental histories from skeletal diaries —
947 Advances in sclerochronology. *Palaeogeography, Palaeoclimatology, Palaeoecology* **373**, 1–5.

948 Schöne B. R., Zhang Z., Radermacher P., Thébault J., Jacob D. E., Nunn E. V. and Maurer A.-F.
949 (2011) Sr/Ca and Mg/Ca ratios of ontogenetically old, long-lived bivalve shells (*Arctica islandica*) and
950 their function as paleotemperature proxies. *Palaeogeography, Palaeoclimatology, Palaeoecology* **302**,
951 52–64.

952 Sinnesael M., De Vleeschouwer D., Zeeden C., Batenburg S. J., Da Silva A.-C., de Winter N. J.,
953 Dinarès-Turell J., Drury A. J., Gambacorta G. and Hilgen F. J. (2019) The Cyclostratigraphy
954 Intercomparison Project (CIP): consistency, merits and pitfalls. *Earth-Science Reviews*, 102965.

955 Sosdian S., Gentry D. K., Lear C. H., Grossman E. L., Hicks D. and Rosenthal Y. (2006) Strontium to
956 calcium ratios in the marine gastropod *Conus ermineus*: Growth rate effects and temperature
957 calibration. *Geochemistry, Geophysics, Geosystems* **7**.

958 Steuber T., Rauch M., Masse J.-P., Graaf J. and Malkoč M. (2005) Low-latitude seasonality of
959 Cretaceous temperatures in warm and cold episodes. *Nature* **437**, 1341–1344.

960 Superville P.-J., De Winter N., Phung A. T., Proix N., Baeyens W. and Gao Y. (2017) Radial metal
961 concentration profiles in trees growing on highly contaminated soils. *Chemosphere* **172**, 80–88.

962 Tarutani T., Clayton R. N. and Mayeda T. K. (1969) The effect of polymorphism and magnesium
963 substitution on oxygen isotope fractionation between calcium carbonate and water. *Geochimica et*
964 *Cosmochimica Acta* **33**, 987–996.

965 Tierney, J. E., Poulsen, C. J., Montañez, I. P., Bhattacharya, T., Feng, R., Ford, H. L., Hönnisch, B.,
966 Inglis, G. N., Petersen, S. V., Sahoo, N., Tabor, C. R., Thirumalai, K., Zhu, J., Burls, N. J., Foster, G.,
967 L., Goddérés, Y., Huber, B. T., Ivany, L. C., Turner, S. K., Lunt, D. J., McElwain, J. C., Mills, B. J. W.,
968 Otto-Bliesner, B. L., Ridgwell, A., and Zhang, Y. G.: Past climates inform our future, 370,
969 <https://doi.org/10.1126/science.aay3701>, 2020.

970 Treble P. C., Schmitt A. K., Edwards R. L., McKeegan K. D., Harrison T. M., Grove M., Cheng H. and
971 Wang Y. J. (2007) High resolution Secondary Ionisation Mass Spectrometry (SIMS) $\delta^{18}\text{O}$ analyses of
972 Hulu Cave speleothem at the time of Heinrich Event 1. *Chemical Geology* **238**, 197–212.

973 Ullmann C. V., Böhm F., Rickaby R. E., Wiechert U. and Korte C. (2013) The Giant Pacific Oyster
974 (*Crassostrea gigas*) as a modern analog for fossil ostreoids: isotopic (Ca, O, C) and elemental (Mg/Ca,
975 Sr/Ca, Mn/Ca) proxies. *Geochemistry, Geophysics, Geosystems* **14**, 4109–4120.

976 Ullmann C. V. and Korte C. (2015) Diagenetic alteration in low-Mg calcite from macrofossils: a review.
977 *Geological Quarterly* **59**, 3–20.

978 Ullmann C. V., Wiechert U. and Korte C. (2010) Oxygen isotope fluctuations in a modern North Sea
979 oyster (*Crassostrea gigas*) compared with annual variations in seawater temperature: Implications for
980 palaeoclimate studies. *Chemical Geology* **277**, 160–166.

981 Urban F. E., Cole J. E. and Overpeck J. T. (2000) Influence of mean climate change on climate
982 variability from a 155-year tropical Pacific coral record. *Nature* **407**, 989–993.

983 Urey H. C. (1948) Oxygen Isotopes in Nature and in the Laboratory. *Science* **108**, 489–496.

984 Van Rampelbergh M., Verheyden S., Allan M., Quinif Y., Keppens E. and Claeys P. (2014) Seasonal
985 variations recorded in cave monitoring results and a 10 year monthly resolved speleothem $\delta^{18}\text{O}$ and
986 $\delta^{13}\text{C}$ record from the Han-sur-Lesse cave, Belgium. *Climate of the Past Discussions* **10**, 1821–1856.

987 Vansteenberghe S., Verheyden S., Cheng H., Edwards R. L., Keppens E. and Claeys P. (2016)
988 Paleoclimate in continental northwestern Europe during the Eemian and early Weichselian (125–
989 97 ka): insights from a Belgian speleothem. *Clim. Past* **12**, 1445–1458.

990 Vansteenberghe S., Winter N. de, Sinnesael M., Verheyden S., Goderis S., Malderen S. J. M. V.,
991 Vanhaecke F. and Claeys P. (2019) Reconstructing seasonality through stable isotope and trace
992 element analysis of the Proserpine stalagmite, Han-sur-Lesse Cave, Belgium: indications for climate-
993 driven changes during the last 400 years. *Climate of the Past Discussions*, 1–32.

994 Verheyden S., Baele J.-M., Keppens E., Genty D., Cattani O., Cheng H., LAWRENCE E., ZHANG H.,
995 Van Strijdonck M. and Quinif Y. (2006) The Proserpine stalagmite (Han-Sur-Lesse Cave, Belgium):
996 preliminary environmental interpretation of the last 1000 years as recorded in a layered speleothem.
997 *Geologica Belgica*.

998 de Villiers S., Nelson B. K. and Chivas A. R. (1995) Biological controls on coral Sr/Ca and delta18O
999 reconstructions of sea surface temperatures. *Science* **269**, 1247.

1000 von der Heydt, A. S., Ashwin, P., Camp, C. D., Crucifix, M., Dijkstra, H. A., Ditlevsen, P., and Lenton,
1001 T. M.: Quantification and interpretation of the climate variability record, *Global and Planetary Change*,
1002 [197, 103399, https://doi.org/10.1016/j.gloplacha.2020.103399](https://doi.org/10.1016/j.gloplacha.2020.103399), 2021.

1003 Wang Y. J., Cheng H., Edwards R. L., An Z. S., Wu J. Y., Shen C.-C. and Dorale J. A. (2001) A High-
1004 Resolution Absolute-Dated Late Pleistocene Monsoon Record from Hulu Cave, China. *Science* **294**,
1005 2345–2348.

1006 Watkins J. M., Hunt J. D., Ryerson F. J. and DePaolo D. J. (2014) The influence of temperature, pH,
1007 and growth rate on the delta18O composition of inorganically precipitated calcite. *Earth and Planetary
1008 Science Letters* **404**, 332–343.

1009 Wilkinson B. H. and Ivany L. C. (2002) Paleoclimatic inference from stable isotope profiles of
1010 accretionary biogenic hardparts – a quantitative approach to the evaluation of incomplete data.
1011 *Palaeogeography, Palaeoclimatology, Palaeoecology* **185**, 95–114.

1012 de Winter N., Vellekoop J., Vorsselmans R., Golreihan A., Soete J., Petersen S., Meyer K., Casadio
1013 S., Speijer R. and Claeys P. (2018) An assessment of latest Cretaceous *Pycnodonte vesicularis*
1014 (Lamarck, 1806) shells as records for palaeoseasonality: a multi-proxy investigation. *Climate of the
1015 Past* **14**, 725–749.

1016 de Winter N. J., Agterhuis T. and Ziegler M. (2021) Optimizing sampling strategies in high-resolution
1017 paleoclimate records. *Climate of the Past* **17**, 1315–1340.

1018 de Winter N. J., Goderis S., Dehairs F., Jagt J. W., Fraaije R. H., Van Malderen S. J., Vanhaecke F.
1019 and Claeys P. (2017) Tropical seasonality in the late Campanian (late Cretaceous): Comparison
1020 between multiproxy records from three bivalve taxa from Oman. *Palaeogeography, Palaeoclimatology,
1021 Palaeoecology* **485**, 740–760.

1022 de Winter N. J., Goderis S., Malderen S. J. M. V., Sinnesael M., Vansteenberghe S., Snoeck C., Belza
1023 J., Vanhaecke F. and Claeys P. (2020a) Subdaily-Scale Chemical Variability in a *Torreites Sanchezi*
1024 Rudist Shell: Implications for Rudist Paleobiology and the Cretaceous Day-Night Cycle.
1025 *Paleoceanography and Paleoclimatology* **35**, e2019PA003723.

1026 de Winter N. J., Ullmann C. V., Sørensen A. M., Thibault N., Goderis S., Van Malderen S. J. M.,
1027 Snoeck C., Goolaerts S., Vanhaecke F. and Claeys P. (2020b) Shell chemistry of the boreal
1028 Campanian bivalve *Rastellum diluvianum* (Linnaeus, 1767) reveals temperature
1029 seasonality, growth rates and life cycle of an extinct Cretaceous oyster. *Biogeosciences* **17**, 2897–
1030 2922.

1031 de Winter N. J., Vellekoop J., Clark A. J., Stassen P., Speijer R. P. and Claeys P. (2020c) The giant
1032 marine gastropod *Campanile giganteum* (Lamarck, 1804) as a high-resolution archive of seasonality in
1033 the Eocene greenhouse world. *Geochemistry, Geophysics, Geosystems* **21**, e2019GC008794.

1034 de Winter N. J., Agterhuis T. and Ziegler M. (2021a) Optimizing sampling strategies in high-resolution
1035 paleoclimate records. *Climate of the Past* **17**, 1315–1340.

1036 de Winter, N. J., Dämmер, L. K., Falkenroth, M., Reichart, G.-J., Moretti, S., Martínez-García, A.,
1037 Höche, N., Schöne, B. R., Rodiouchkina, K., Goderis, S., Vanhaecke, F., van Leeuwen, S. M., and
1038 Ziegler, M. (2021b) Multi-isotopic and trace element evidence against different formation pathways for
1039 oyster microstructures. *Geochimica et Cosmochimica Acta*, **308**, 326–352.
1040 <https://doi.org/10.1016/j.gca.2021.06.012>.

1041 Xu C., Zheng H., Nakatsuka T., Sano M., Li Z. and Ge J. (2016) Inter-and intra-annual tree-ring
1042 cellulose oxygen isotope variability in response to precipitation in Southeast China. *Trees* **30**, 785–
1043 794.

1044 Yan H., Liu C., An Z., Yang W., Yang Yuanjian, Huang P., Qiu S., Zhou P., Zhao N., Fei H., Ma X., Shi
1045 G., Dodson J., Hao J., Yu K., Wei G., Yang Yanan, Jin Z. and Zhou W. (2020) Extreme weather
1046 events recorded by daily to hourly resolution biogeochemical proxies of marine giant clam shells.
1047 *PNAS* **117**, 7038–7043.

1048 Zhu F., Emile-Geay J., McKay N. P., Hakim G. J., Khider D., Ault T. R., Steig E. J., Dee S. and
1049 Kirchner J. W. (2019) Climate models can correctly simulate the continuum of global-average
1050 temperature variability. *PNAS* **116**, 8728–8733.

1051